SAND2016-9793

SANDIA REPORT

2016-9793
Unlimited Release
Printed September 2016

Modeling primary atomization of liquid fuels using a multiphase DNS/LES Approach

Marco Arienti, François Doisneau, Joe Oefelein

Prepared by
Sandia National Laboratories
Albuquerque, New Mexico 87185 and Livermore, California 94550

Sandia National Laboratories is a multi-program laboratory managed and operated by Sandia Corporation, a wholly owned subsidiary of Lockheed Martin Corporation, for the U.S. Department of Energy's National Nuclear Security Administration under contract DE-AC04-94AL85000.

Issued by Sandia National Laboratories, operated for the United States Department of Energy by Sandia Corporation.

Available to DOE and DOE contractors from
U.S. Department of Energy
Office of Scientific and Technical Information
P.O. Box 62
Oak Ridge, TN 37831

Telephone: (865) 576-8401
Facsimile: (865) 576-5728
E-Mail: reports@adonis.osti.gov
Online ordering: http://www.osti.gov/bridge

Available to the public from
U.S. Department of Commerce
National Technical Information Service
5285 Port Royal Rd
Springfield, VA 22161

Telephone: (800) 553-6847
Facsimile: (703) 605-6900
E-Mail: orders@ntis.fedworld.gov
Online ordering: http://www.ntis.gov/help/ordermethods.asp?loc=7-4-0#online

2016-9793
Unlimited Release
Printed September 2016

Modeling primary atomization of liquid fuels using a multiphase DNS/LES Approach

Marco Arienti, François Doisneau, Joe Oefelein

Abstract

We report on the development of a model framework to simulate spray flames from direct injection of liquid fuel into an automotive cylinder engine. The approach to this challenging problem was twofold. On one hand, the interface-capturing multiphase computer code CLSVOF was used to resolve the rapidly evolving, topologically convoluted interfaces that separate the liquid fuel from the gas at injection: the main challenges to address were the treatment of the high-pressure flow inside the injector, which required the inclusion of compressibility effects; and the computational framework necessary to achieve a Direct Numerical Simulation (DNS) level of accuracy. On the other hand, the scales of turbulent fuel mixing and combustion in the cylinder engine were addressed by the high-performance computer code Raptor within the Large Eddy Simulation (LES) framework. To couple the two computational methods, a novel methodology was developed to describe the dense spray dynamics in Raptor from the assigned spray size distribution and dispersion angle derived from CLSVOF. This new, independent Eulerian Multi-Fluid (EMF) spray module was developed based on the kinetic description of a system of droplets as a pressure-less gas; as we will show, it was demonstrated to efficiently render the near-nozzle coupling in mass, momentum, and energy with the carrier gas phase.

Acknowledgment

Support by Sandia National Laboratories' Laboratory Directed Research and Development (LDRD) program is gratefully acknowledged. Sandia National Laboratories is a multi-program laboratory managed and operated by Sandia Corporation, a wholly owned subsidiary of Lockheed Martin Corporation, for the U.S. Department of Energy's National Nuclear Security Administration under contract DE-AC04-94AL85000.

Contents

List of Figures

List of Tables

Nomenclature

ASOI After start of injection

CFL Courant-Friederichs-Lewy number

CLSVOF Coupled Level-Set/Volume of Fluid

DNS Direct numerical simulation

DSMC Direct simulation Monte-Carlo

ECN Engine Combustion Network

EMF Eulerian Multi-Fluid

FSL-LP Forward Semi-Lagrangian with Linear Projection

LES Large Eddy Simulation

NDF Number Density Function

PGD Pressureless Gas Dynamics

RANS Reynolds-average Navier-Stokes

Chapter 1

Modeling strategy

This project is restricted to the study of direct fuel injection under sub-critical conditions, where an interface can be distinguished between liquid and gas phase and separate equations of state describe the two fluids. For a discussion on the transition from processes exhibiting classical two-phase spray atomization phenomena (the term refers to the formation of spray from a liquid jet or sheet) to super-critical, single-phase, diffusion-dominated mixing, the reader is referred to [18] and [19].

In sub-critical fuel injection, it is convenient to characterize the local state of the liquid phase as either continuous (liquid core and ligaments) or dispersed (dense and dilute spray). The distinction not strict since a churning liquid core, atomizing ligaments, and coalescing drops in a dense spray are difficult to theoretically characterize and experimentally identify. In any case, the near-nozzle region is characterized by high mass loadings and volume fractions of liquid. This situation is hereafter referred to as dense spray. The characteristics and the variability of engine combustion are believed to be controlled by small-scale phenomena (cavitation, turbulence, local spray properties) in the fuel injector and near-nozzle region. How these perturbations amplify, as the mixing layer within the fuel sprays grows and the drops form and vaporize, cannot be yet estimated from a reduced-order model nor, because of a combination of extreme conditions and inaccessibility, observed in an experiment.

High-fidelity, high-resolution simulations can potentially unlock our understanding of these multiscale, multiphysics processes, but face substantial obstacles. The multiphase sharp-interface formalism used in this project can track fuel injection on a time-scale of nanoseconds, capturing fragmenting liquid interfaces with micrometer resolution near the injector. This capability is unique since it does not require pre-existing knowledge of the injector device or the availability of an appropriate model for spray formation. However, a Direct Numerical Simulation (DNS) approach spanning nozzle, spray, and flame – with no model assumed for spray formation, turbulent mixing, and combustion – is intractable. The Large Eddy Simulation (LES) framework, on the other hand, can treat the full range of multidimensional scales in turbulent reacting flows in a computationally feasible manner. Large energetic scales in the flow are resolved, while small subgrid scales are modeled in homogenous isotropic flow. However, modeling fuel atomization in the LES framework poses new challenges caused by dynamically evolving interface boundaries.

We have devised a twofold strategy based on the connection of two purposely extended simulation capabilities:

- a DNS code for primary atomization: the multiphase Navier-Stokes solver (CLSVOF) [41];
- a LES code for the simulation of mixing and turbulent combustion: the low dissipation,

multicomponent Navier-Stokes solver (Raptor) [52] .

This strategy is illustrated in Fig. 1.1, where the domain of competence of the two codes is separately displayed in the upper and bottom panels. This LDRD project supported the development of an Eulerian Multi-Fluid technique for sprays in Raptor. The numerical strategy was developed in [28] and [29], where it was shown to be accurate in coupling the dispersed spray phase with the gas phase. While taking advantage of the existing data structure and solver capability of RAPTOR for the carrier phase, care was taken in making the implementation of this concept modular, so that the same technique can be directly exported to any multicomponent code. LDRD funding also supported the extension of CLSVOF to simulate compressible flow and thermal transfer inside the injector. The general framework was introduced in [41], but the implementation of the complete equation of state for n-dodecane (a surrogate of Diesel fuel) and the campaign of validation studies with data from the Engine Combustion Network were carried out within this project. Results were published in [2] and [1].

Because most of the details are already included in the aforementioned publications, this report is focused on motivating the numerical choices that were adopted and on explaining the links between the LES and the DNS simulations. Specifically, the Eulerian Multi-Fluid approach is described as a general approach in Chapters 2 and 3 and then specialized to direct fuel injection in Chapter 4. The final chapter is devoted to the project target of a spray flame simulation, presented in a staged approach: first the DNS simulation by CLSVOF of the internal and external flow of the injector, leading to primary atomization and to the extraction of a droplet population; second, intermediate LES cases of monodisperse non-evaporating and evaporating sprays with Eulerian Multi-Fluid in RAPTOR starting from the orifice exit as boundary condition; and, third, the simulation of the polydisperse spray extracted from CLSVOF up to autoignition.

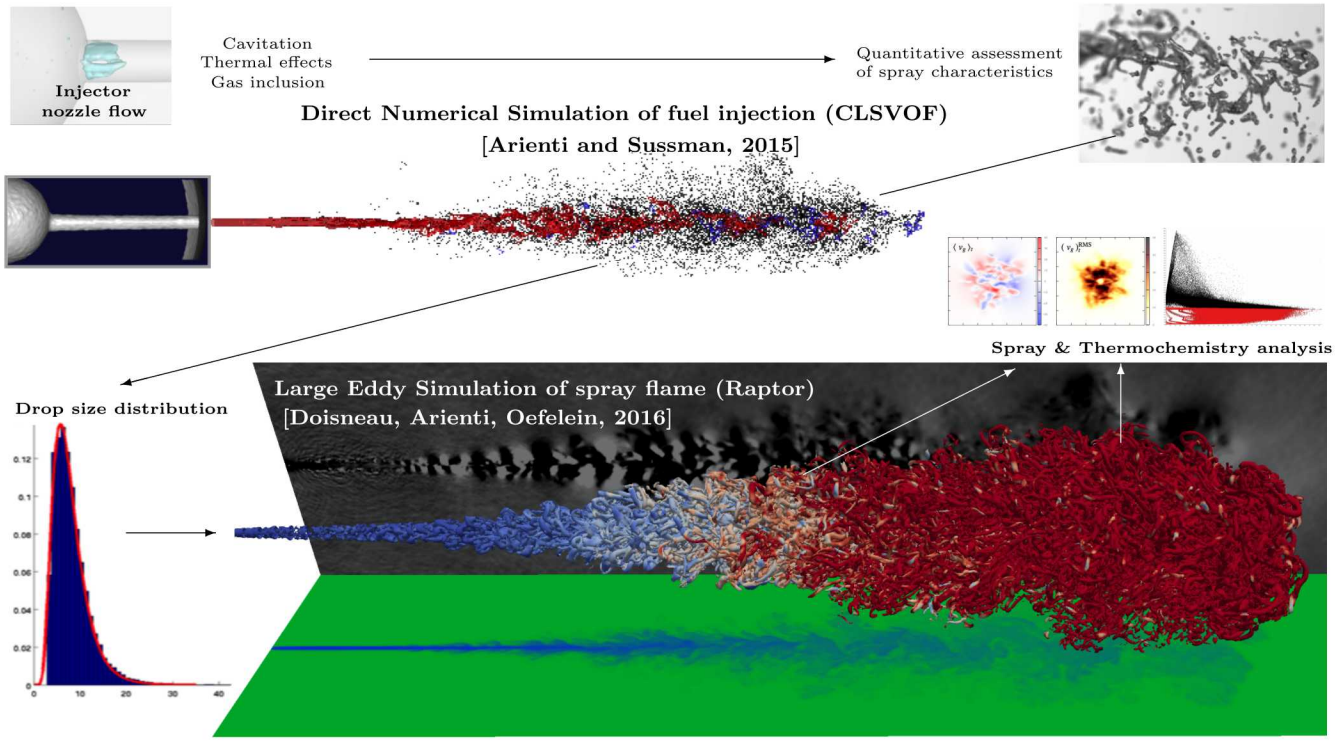

Figure 1.1. Schematic of DNS/LES strategy for fuel injection.

Chapter 2

Introduction to Eulerian spray modeling

2.1 Available options for multiphase flow

Well-established strategies to model a discrete distribution of particles in the carrier phase can be categorized as: Stochastic Lagrangian Spray, or Direct Simulation Monte Carlo (DSMC) [7]; Eulerian Spray [46]; Discrete Particle Simulation (DPS) [65]; Particle-Resolved (PR) DPS [64]; and Eulerian Liquid, with or without explicit interface-capturing [50, 2]. These models can be coupled to the carrier phase using volume sources (for the three first approaches) or interface boundary conditions (for the last two). With each of these approaches, although at different scales, there will be large density, momentum, and temperature gradients, as well as rapid phase changes. Capturing these gradients is of paramount importance to render the physics of the spray since i) the transfer rates depend on the local liquid mass loading, and ii) the fronts do not smooth out with time compared to gas dynamics where acoustics and diffusion tend to bring back a balance fast: spray ignition, combustion, and flame extinction are very sensitive to the steepness of the droplet cloud density fronts, as suggested by Direct Numerical Simulation of droplet evaporation in turbulent flow [56].

Table 2.1. Nomenclature of various models for transport in physical space. Velocity closures include PGD: pressureless gas dynamics [20], IG/AG/MG: isotropic/anisotropic/multi-Gaussian [69], CQMOM: conditional quadrature method of moments [74].

	Formalism	Hyperbolicity	Compressibility	Pros	Cons
DPS	Lagrangian	yes, linear	hyper	deterministic	cost, initial/boundary conditions
Kinetic	Eulerian	yes, linear	hyper	flexible	high dimensionality (7D/9D)
Fluid Gas	Eulerian	yes, non-linear	high	4D	
Liquid	Eulerian	yes, non-linear	low	4D	
Spray PGD, CQMOM	Eulerian	weakly, non-linear	hyper	5D	produces δ-shocks
IG, AG, MG	Eulerian	yes, non-linear	hyper	5D	"equilibrium" velocities
DSMC	Lagrangian	yes, linear	hyper	non-equilibrium	stochastic (converges as $\sqrt{N_p}$)

Table 2.1 summarizes the models for transport in physical space. Models below the double line can all be derived from a kinetic equation, either the Boltzmann or the Williams-Boltzmann

equation [72]. In other words, the kinetic description of a spray is foundational to all Eulerian Spray models and to DSMC: Eulerian models then trade deterministic solutions for a statistical description of local velocities at equilibrium; e.g., monokinetic or Gaussian, whereas the DSMC model trades linearity and ease of transport implementation part for a sublinear convergence of the statistics with the number of parcels.

2.2 Kinetic equation for sprays

2.2.1 Fluid-kinetic model

We consider a spray; i.e., disperse liquid structures suspended in a carrier gas. It is described with a fluid-kinetic model [72] using a set of continuous fluid equations for the gas (compressible Navier-Stokes system), which is strongly coupled to a kinetic equation for the disperse phase. The internal coordinates translate the degrees of freedom of particles, which are now droplets, and are the velocity vector, droplet temperature, and radius $(\boldsymbol{c}, \theta, r)$. Coupling is achieved through mass, momentum, and enthalpy source terms accounting for evaporation, drag, and heat transfer in a conservative way. This description is sufficient if the volume fraction of the disperse phase is not too high, and it can be easily closed if the liquid structures are spherical enough [46, 20]. The fluid-kinetic model is given by the system

$$\begin{cases} \partial_t\left(\rho_g Y_l\right) + \partial_{\boldsymbol{x}}\left(\rho_g Y_l \boldsymbol{u}_g\right) & = -\partial_{\boldsymbol{x}}\mathbf{q}_l + \omega_l, & l \in [\![1; N_{\text{species}}]\!],\ l \neq f \\ \partial_t\left(\rho_g Y_f\right) + \partial_{\boldsymbol{x}}\left(\rho_g Y_f \boldsymbol{u}_g\right) & = -\partial_{\boldsymbol{x}}\mathbf{q}_f + \omega_f + \displaystyle\int_{\boldsymbol{c},\theta,r} \Big(m(r)\mathrm{E}\Big) f \mathrm{d}\boldsymbol{c}\mathrm{d}\theta\mathrm{d}r & \\ \partial_t\left(\rho_g \boldsymbol{u}_g\right) + \partial_{\boldsymbol{x}}\left(\rho_g \boldsymbol{u}_g \otimes \boldsymbol{u}_g\right) & = -\partial_{\boldsymbol{x}} p - \partial_{\boldsymbol{x}}\mathbf{S} + \displaystyle\int_{\boldsymbol{c},\theta,r} \Big(-\mathbf{F} + \boldsymbol{c}\mathrm{E}\Big) f \mathrm{d}\boldsymbol{c}\mathrm{d}\theta\mathrm{d}r & \\ \partial_t\left(\rho_g e_g\right) + \partial_{\boldsymbol{x}}\left(\rho_g e_g \boldsymbol{u}_g\right) & = -p\partial_{\boldsymbol{x}}\boldsymbol{u}_g - \partial_{\boldsymbol{x}}\mathbf{q} + \displaystyle\int_{\boldsymbol{c},\theta,r} \Big(-\mathrm{H} - \mathbf{F}\cdot(\boldsymbol{u}_g - \boldsymbol{c}) + h(\theta, r)\mathrm{E}\Big) f \mathrm{d}\boldsymbol{c}\mathrm{d}\theta\mathrm{d}r & \\ \partial_t f + \partial_{\boldsymbol{x}}\left(\boldsymbol{c} f\right) + \partial_{\boldsymbol{c}}\left(\mathbf{F} f\right) + \partial_\theta\left(\mathrm{H} f\right) + \partial_r\left(\mathrm{E} f\right) = \mathfrak{B} + \mathfrak{C}, & \end{cases} \tag{2.1}$$

where the indices l refer to the chemical species together with index f which refers to the one gas species composing the evaporation product from the liquid. The various source terms describe chemical reaction (ω_f and all the ω_l), evaporation (E), drag ($\mathbf{F}$), heating (H), break-up ($\mathfrak{B}$), and coalescence ($\mathfrak{C}$). The integrals defining the coupling terms in the Navier-Stokes equation are computed from the knowledge of drop closures, $m(r)$ being the mass and $h(r, \theta)$ being the enthalpy. For the sake of legibility we have omitted use of filter notation associated with LES and we refer the reader to the literature for turbulent fluxes to be added in the species flux $\mathbf{q}_l$, stress tensor $\mathbf{S}$, and heat flux $\mathbf{q}$. As for the effect of filtering on the disperse phase equation, we do not account for it and leave this important research topic for later [27]. Any effect of the highly-loaded disperse phase on the filtered terms in the Navier-Stokes system [34] is left aside for the same reasons. We also neglect ω_f, ω_l, $\mathfrak{B}$, and $\mathfrak{C}$ in the present study since they do not contribute to gas-liquid coupling, keeping in mind that the present method can be directly extended to the treatment of these terms. Here we focus on evaporation, drag, and heating as they are inducing the coupling of interest between the two phases. Note that n the above fluid-kinetic Eq. (2.1) equation, the disperse phase. The number density function (NDF) $f(t, \boldsymbol{x}; \boldsymbol{c}, \theta, r)$ has 5D in addition to the 4D of space and time.

2.3 Eulerian modeling

Eulerian methods require the reduction of the phase space size to be tractable. In the case of the modeling and simulation of spray flames [20] and of aluminum particles in solid rocket motors [26], various assumptions can be made on the velocities of the particles such as the monokinetic assumption [20] or Gaussian closures [69]. In general, conditioning assumptions between phase space variables bring in new systems of equations to approximate the original kinetic equation. Each set of assumptions used to reduce the size of a kinetic problem will require the introduction of a dedicated transport method. "Fluids" of particles are also highly compressible [23] because the spatial waves in the modeled system are slower and weaker than in actual gas dynamics (where they arise from molecular collisions). While most of the past 60 years' efforts on hyperbolic systems [35, 68, 59, 13] were oriented towards gas dynamics (incompressible, low Mach, supersonic, hypersonic), the resulting schemes are not suitable for disperse phase flows. Dedicated numerical methods are therefore required to treat such hypercompressible transport in physical space [20, 43, 70, 58]. Eulerian methods have been applied with success to mechanical engineering problems, especially when the coupling is strong, through two-way momentum and heat transfers or through evaporation. Examples of applications are gas turbine ignition [8], Diesel spray polydisperse evaporation [31, 42] and combustion LES [66], hydroacoustic [26] and thermoacoustic [60] instabilities, and fluidized beds [33]. Eulerian methods have been acknowledged for their good coupling and parallel properties in the spray community [8, 24].

2.3.1 Semi-kinetic models

The reduction of dimensionality of the NDF through assumptions on velocity distributions leads to a wealth of Eulerian systems, so-called hydrodynamic models. For sprays whose dynamics strongly depends on the droplet sizes, a reduction methodology relies on size-conditioning and shape-presuming [46]. After size conditioning, the shape-presuming reduction effort can be thought of two distinct modeling steps: i) the velocity treatment (on a size-conditioned basis) that leads to the various models for transport in physical space and ii) the size treatment.

The system with size-conditioned velocities is sometimes referred to as semi-kinetic because the size variable remains a continuous one, adding a dimension compared to usual hydrodynamic models [46]. Assuming perfectly correlated velocities, i.e., the monokinetic closure,

$$f(t,\boldsymbol{x};\boldsymbol{c},\theta,r) \approx \sum_{k=1}^{N_{\text{sec}}} \kappa_k(t,\boldsymbol{x};r)\delta(\boldsymbol{c}-\boldsymbol{u}_k(t,\boldsymbol{x}))\delta(\theta - T_k(t,\boldsymbol{x})) \tag{2.2}$$

leads to a Eulerian system and is valid as long as r is below a critical size; above that critical size, trajectory crossings may occur in vortical and stretched regions of the flow. The monikinetic closure can be seen as the zero-temperature limit of the Maxwell-Boltzmann distribution and leads to PGD for which the Forward Semi-Lagrangian (FSL) scheme described later has been based on. PGD is relevant for particles/drops because the gas drag force tends to correlate the velocities locally in physical space.

For sprays, the monokinetic assumption can been relaxed, leading to models accounting for statistical trajectory crossings, e.g., caused by turbulence [69, 11]. Yet for these closures, the pressure (tensor) that builds up in inertial areas due to crossings usually remains weak compared

to advection so that FSL retains relevance for inertial drop transport models. For simplicity, we apply the monokinetic assumption, while seeking accuracy on the droplet size by discretizing the size phase space.

2.3.2 Eulerian Multi-Fluid model

For the size treatment step ii), we consider a finite volume discretization referred to as Multi-Fluid, which is, in fact, an extension of sectional methods that can include sections with independent velocity treatments [46]. The entire size distribution can be accounted for by combined moment and Multi-Fluid methods. It can be efficiently transported with arbitrary accuracy, allowing one to render the missing global size moments; e.g., the Sauter Mean Diameter. The Multi-Fluid approach can uniquely reconstruct any NDF from the knowledge of a set of moments in size, velocity, and temperature,

$$\begin{pmatrix} m_{k,0} \\ \dots \\ m_{k,n} \\ m_{k,3}\boldsymbol{u}_k \\ m_{k,3}T_k \end{pmatrix}(t,\boldsymbol{x}) = \int_{r_{k-1}}^{r_k}\int_{\mathbb{R}^+}\int_{\mathbb{R}^3} \begin{pmatrix} 1 \\ \dots \\ r^n \\ r^3\boldsymbol{c} \\ r^3\theta \end{pmatrix} f(t,\boldsymbol{x};\boldsymbol{c},\theta,r)\mathrm{d}\boldsymbol{c}\mathrm{d}\theta\mathrm{d}r, \qquad k\in[\![1;N_{\mathrm{sec}}]\!] \tag{2.3}$$

where the number of moments n is related to the number of unknown parameters in the shapes κ_k that are presumed in each section k [47] The equivalence above holds as long as $r_0 < r_1 < \dots < r_{N_{\mathrm{sec}}} = +\infty$ is a partition of the size phase space. The N_{sec} intervals are referred to as the sections [46, 25]. The Multi-Fluid modeling strategy has been applied to engine sprays [20] and specific extensions were considered [30, 42, 31] in cases where the numerical setup was limiting local drop concentrations to the dilute spray regime; e.g., by injecting liquid downstream of the nozzle. The strategy and numerics devised here focus on capturing near-nozzle scales and connecting dense spray dynamics to a dilute reacting spray. A review of spray injection and autoignition simulations [29] gives practical arguments to support this strategy.

Choosing two moments is typically a good trade-off [26] for polydisperse problems with diverse drop dynamics. In the following, we therefore resort to two moments in size per section. These are number and mass $(m_{k,0}, m_{k,3})$, simply noted (n_k, m_k), so we need to account for 6 scalar moments $(n_k, m_k, m_k\boldsymbol{u}_k, m_kT_k)$ per section. The disperse phase is therefore described by $6N_{\mathrm{sec}}$ scalar Eulerian fields in 4D, instead of a scalar 9D problem. The final governing system of equations then reads

$$\left\{\begin{array}{ll}
\partial_t(\rho_g Y_l) + \partial_{\boldsymbol{x}}(\rho_g Y_l \boldsymbol{u}_g) & = -\partial_{\boldsymbol{x}}\mathbf{q}_l, \qquad\qquad l\in[\![1;N_{\mathrm{species}}]\!],\ l\neq f \\
\partial_t(\rho_g Y_f) + \partial_{\boldsymbol{x}}(\rho_g Y_f \boldsymbol{u}_g) & = -\partial_{\boldsymbol{x}}\mathbf{q}_f + \sum_k \mathrm{E}_k^{m-g} \\
\partial_t(\rho_g \boldsymbol{u}_g) + \partial_{\boldsymbol{x}}(\rho_g \boldsymbol{u}_g\otimes\boldsymbol{u}_g) & = -\partial_{\boldsymbol{x}}p - \partial_{\boldsymbol{x}}\mathbf{S} + \sum_k \left(-\mathbf{F}_k + \boldsymbol{u}_k\mathrm{E}_k^{m-g}\right) \\
\partial_t(\rho_g e_g) + \partial_{\boldsymbol{x}}(\rho_g e_g \boldsymbol{u}_g) & = -p\partial_{\boldsymbol{x}}\boldsymbol{u}_g - \partial_{\boldsymbol{x}}\mathbf{q} + \sum_k \left(-\mathrm{H}_k + \mathbf{F}_k(\boldsymbol{u}_g-\boldsymbol{u}_k) + h_k\mathrm{E}_k^{m-g}\right) \\
\left.\begin{array}{ll}
\partial_t n_k + \partial_{\boldsymbol{x}}(n_k\boldsymbol{u}_k) & = \mathrm{E}_{k+1}^n - \mathrm{E}_k^n \\
\partial_t m_k + \partial_{\boldsymbol{x}}(m_k\boldsymbol{u}_k) & = \mathrm{E}_{k+1}^m - (\mathrm{E}_k^m + \mathrm{E}_k^{m-g}) \\
\partial_t(m_k\boldsymbol{u}_k) + \partial_{\boldsymbol{x}}(m_k\boldsymbol{u}_k\otimes\boldsymbol{u}_k) & = \mathbf{F}_k + \boldsymbol{u}_{k+1}\mathrm{E}_{k+1}^m - \boldsymbol{u}_k(\mathrm{E}_k^m + \mathrm{E}_k^{m-g}) \\
\partial_t(m_k h_k) + \partial_{\boldsymbol{x}}(m_k h_k\boldsymbol{u}_k) & = \mathrm{H}_k + h_{k+1}\mathrm{E}_{k+1}^m - h_k(\mathrm{E}_k^m + \mathrm{E}_k^{m-g})
\end{array}\right\} k\in[\![1;N_{\mathrm{sec}}]\!].
\end{array}\right. \tag{2.4}$$

This is referred to as the Eulerian Multi-Fluid model.

2.3.3 Illustration of Lagrangian vs. Eulerian Multi-Fluid modeling for sprays

As a demonstration of the difference between the EMF approach and the traditional Lagrangian, or DSMC, approach, we consider a droplet cloud that is one-way coupled to a prescribed gas field. The choice of one-way coupling is motivated by the need to establish a comparison between the two discretizations. The gas field is a slice of a circular jet that was computed offline and then discretized over a self-similarly stretched grid. The spray jet boundary condition is prescribed by the Downstream Inflow Turbulent Boundary Conditions (DITurBC) to emulate the outcome of primary atomization of a fuel spray for piston engine simulations [49]. Drag is evaluated by interpolating the gas velocity values at particle locations in DSMC and at the regularly spaced grid centers in the EMF approach. The same time step, based on the CFL constraint, is used in both calculations. Finally, the number of degrees of freedom to describe the disperse phase is the same: DSMC has 2 million parcels (sampling random initial locations and droplet sizes), while the EMF model has 10 sections (to discretize size phase space) on 0.2 million cells.

The resulting droplet cloud is transient, non-uniform, polydisperse, and tends toward a size-conditioned velocity distribution. A snapshots is displayed in Fig. 2.1: The two results compare very well with each other, and this suggests that the monokinetic assumption in the EMF simulation is justified. The DSMC method exhibits noise on the spatial fields in the depleted regions, or oversampling in region of high parcel concentration, while the Eulerian method is statistically converged by construction. DSMC non-uniformities are driven by the Monte-Carlo initial conditions and they are very difficult to predict and to correct. In return, the EMF field is smoother due to numerical diffusion. The DSMC non-uniformities in number of parcels result in waste of computational resources in the over-sampled regions and in noise in the under-sampled regions as illustrated in Fig. 2.2. Without a redistribution strategy, it can be expected that load-balancing issues could arise in the parallel execution of DSMC. Conversely, issues of load-balancing do not appear in the EMF scheme because the droplets degrees of freedom are linked to the computational cells.

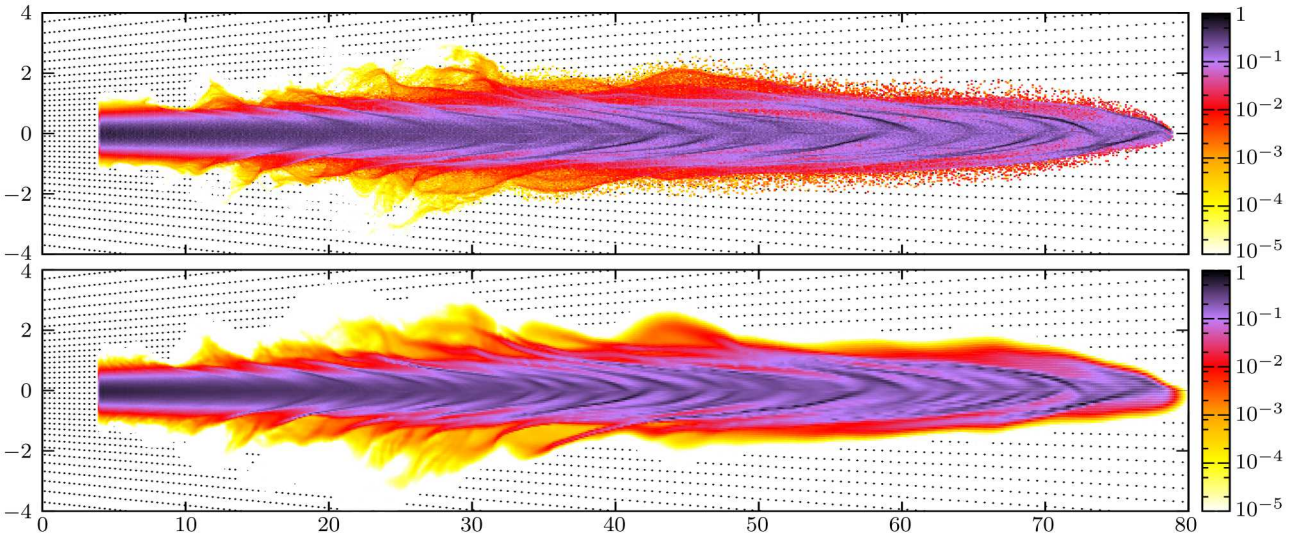

Figure 2.1. Direct fuel injection spray with one-way coupling – Fuel mass concentration normalized by ρ_l with Lagrangian DSMC (top, 2Mparcels) and Hybrid Eulerian-Lagrangian (bottom, 200kcells×10 sections). The black dots are the locations of the gas field cell centers.

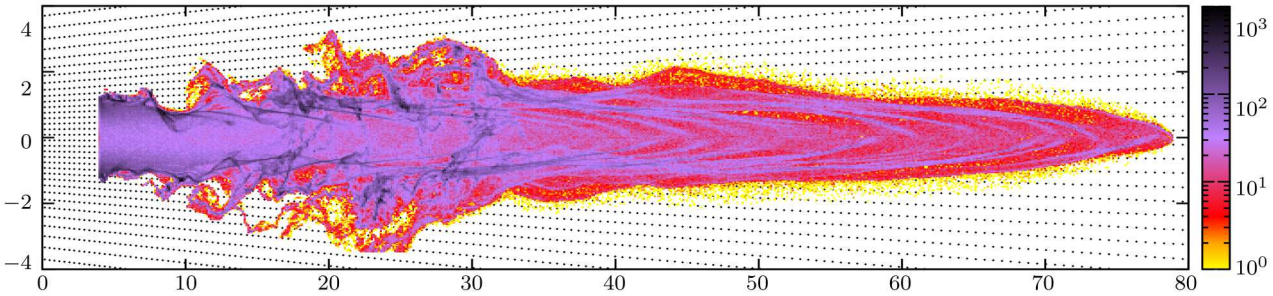

Figure 2.2. Number of numerical parcels per cell with Lagrangian DSMC for the 2D one-way coupled case.

Chapter 3

Eulerian modeling with forward semi-Lagrangian transport

3.1 Description of the scheme

To achieve strong coupling between the carrier and the dispersed phase, it is convenient to perform the transport operation with a method that has Lagrangian features while keeping the data in the form of a deterministic Eulerian field. The calculation of the time evolution of hyperbolic equations by integrating along characteristics of the system, while projecting information back to the Eulerian grid, is referred to as semi-Lagrangian technique. It was introduced by Courant et al. [15] with a forward (explicit) and a backward (implicit) version, the latter being widely used in geosciences for global computations [71, 44, 57, 63, 61] and also in plasma dynamics [21, 12, 62, 36]. Advection-dominated problems, such as passive scalar transport, are good candidates for forward semi-Lagrangian approaches. In the context of disperse phase modeling, a semi-Lagrangian technique is attractive because it is naturally compatible with the weakly-coupled nature of the material elements that are transported; i.e., weak diffusion and collisions, and slow or zero-velocity waves allow the characteristics to remain fairly independent of each other.

An attempt of one-way coupled spray calculation by using a backward semi-Lagrangian method is reported in [53]; more recently, emphasis was put on achieving non-oscillatory high-order schemes for dilute weakly collisional sprays [5]. The connection between semi-Lagrangian schemes and the remeshing process for stochastic Lagrangian methods was established in [14], emphasizing the requirements for achieving conservation properties. These issues become even more significant when strong coupling needs to be modeled, because additional constraints on regularity and oscillations have to be enforced. Thus, semi-Lagrangian approaches appear as a viable strategy to perform the transport of kinetic systems with internally weak coupling and are promising for strongly coupled problems such as dense sprays. The details of the semi-Lagrangian transport scheme are developed next after pointing out the need for operator splitting.

3.1.1 Operator splitting

We apply operator splitting to Eq. (2.4) to use specialized time integration schemes for the different operators [22, 20]. A more complete discussion on splitting, as applied to coupled spray systems, can be found in [26]. At present, we define the three operators illustrated in Fig. 3.1: these are the gas transport $\mathscr{T}_g$, the section transport $\mathscr{T}_k$, where $k \in [\![1; N_{\text{sec}}]\!]$, and the coupling operator $\mathscr{C}$. The latter operator describes how fast the liquid and gas velocities converge locally to an equilibrium

value in a way that conserves the system's momentum.

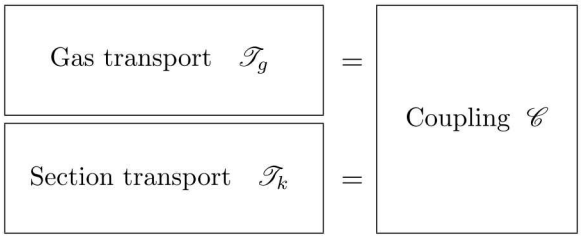

Figure 3.1. Schematic of the splitting strategy.

The transport part of the gas phase, $\mathscr{T}_g$, reduces to the Navier-Stokes system; either explicit, implicit, or mixed time integration strategies can be considered for advancing the solution, with the usual constraints such as Courant-Friederichs-Lewy number (CFL) and Von-Neuman number (VNN) for this mixed hyperbolic-parabolic set of equations. The coupling operator, $\mathscr{C}$, is a set of ODEs

$$\left\{\begin{array}{lll}
\mathrm{d}_t(\rho_g Y_l) & = 0, & l \in [\![1; N_{\text{species}}]\!],\ l \neq f \\
\mathrm{d}_t(\rho_g Y_f) & = \displaystyle\sum_k \mathrm{E}_k^{m-g} & \\
\mathrm{d}_t(\rho_g \boldsymbol{u}_g) & = \displaystyle\sum_k \left(-\mathbf{F}_k + \boldsymbol{u}_k \mathrm{E}_k^{m-g}\right) & \\
\mathrm{d}_t(\rho_g e_g) & = \displaystyle\sum_k \left(-\mathrm{H}_k + \mathbf{F}_k(\boldsymbol{u}_g - \boldsymbol{u}_k) + h_k \mathrm{E}_k^{m-g}\right) & \\
\left.\begin{array}{ll}
\mathrm{d}_t n_k & = \mathrm{E}_{k+1}^n - \mathrm{E}_k^n \\
\mathrm{d}_t m_k & = \mathrm{E}_{k+1}^m - (\mathrm{E}_k^m + \mathrm{E}_k^{m-g}) \\
\mathrm{d}_t(m_k \boldsymbol{u}_k) & = \mathbf{F}_k + \boldsymbol{u}_{k+1}\mathrm{E}_{k+1}^m - \boldsymbol{u}_k(\mathrm{E}_k^m + \mathrm{E}_k^{m-g}) \\
\mathrm{d}_t(m_k h_k) & = \mathrm{H}_k + h_{k+1}\mathrm{E}_{k+1}^m - h_k(\mathrm{E}_k^m + \mathrm{E}_k^{m-g})
\end{array}\right\} & k \in [\![1; N_{\text{sec}}]\!]
\end{array}\right. \tag{3.1}$$

that can be integrated explicitly provided that its time scales are larger than the overall splitting time step Δt.

For the two-way coupled system, it is important to note that the characteristic time with respect to drag becomes smaller with a higher liquid loading. This time is locally of the order of

$$\tau_c = \min_k \left(\frac{\tau^{\boldsymbol{u}}(r_k)}{1 + m_k/\rho_g} \right), \tag{3.2}$$

where $\tau^{\boldsymbol{u}}(r_k)$ is the characteristic time of the drag force $\mathbf{F}_k$. As a consequence, discrepancies that might be introduced by assuming spherical closure on momentum coupling (through the choice of the drag law) do not have a significant impact in the regions where loading is sufficiently high, even though the liquid elements there can be very different from spherical droplets. The same argument applies to heat transfer, with $\tau^T(r_k)$ the characteristic time of the heat transfer H_k. As it will be shown in Section 4.2, in regions dominated by the liquid phase it is sufficient to maintain the field velocities and temperatures close to equilibrium.

To respect the coupling between the dense phase and gas phase, the splitting time step is chosen in our work to be equal to the gas phase time step, following the standard CFL constraint. The transported part of the disperse phase, $\mathscr{T}_k$, reduces to N_{sec} systems

$$\begin{cases} \partial_t n_k + \partial_{\boldsymbol{x}} \left(n_k \boldsymbol{u}_k \right) = 0 \\ \partial_t m_k + \partial_{\boldsymbol{x}} \left(m_k \boldsymbol{u}_k \right) = 0 \\ \partial_t \left(m_k \boldsymbol{u}_k \right) + \partial_{\boldsymbol{x}} \left(m_k \boldsymbol{u}_k \otimes \boldsymbol{u}_k \right) = 0 \\ \partial_t \left(m_k h_k \right) + \partial_{\boldsymbol{x}} \left(m_k h_k \boldsymbol{u}_k \right) = 0 \end{cases} \tag{3.3}$$

with a behavior equivalent to the pressureless gas dynamics [75, 9, 10, 20, 58], although with an additional passive scalar.

3.1.2 Description of the scheme

In the context of operator splitting, the transport of of each of the N_{sec} sections is decoupled from the others, therefore making the adaptation of FSL to the Multi-Fluid model straightforward: a different set of particles p is defined for each section k. The transport of the polydisperse spray is performed first with the scattering mapping

$$\begin{pmatrix} n_k \\ m_k \\ m_k \boldsymbol{u}_k \\ m_k \phi_k \end{pmatrix} (t, \boldsymbol{x}_i) \text{ with } (i,k) \in [\![1; N_{\text{cell}}]\!] \times [\![1; N_{\text{sec}}]\!] \quad \rightarrow \quad \begin{pmatrix} \boldsymbol{x}_p \\ n_p \\ m_p \\ \boldsymbol{u}_p \\ \phi_p \end{pmatrix} (t) \text{ with } p \in [\![1; N_p]\!], \tag{3.4}$$

where $\boldsymbol{x}_p = \boldsymbol{x}_i$, $n_p = n_k(t, \boldsymbol{x}_i)$, $m_p = m_k(t, \boldsymbol{x}_i)$, $\boldsymbol{u}_p = \boldsymbol{u}_k(t, \boldsymbol{x}_i)$, $\phi_p = \phi_k(t, \boldsymbol{x}_i)$; and, second, with the gathering mapping

$$\forall (i,k) \in [\![1; N_{\text{cell}}]\!] \times [\![1; N_{\text{sec}}]\!], \quad \begin{pmatrix} \boldsymbol{x}_i \\ n_{i,k} = \dfrac{1}{m_{i,k}} \displaystyle\sum_{p \in \Omega_{\boldsymbol{x}_i}} w_{pi} n_p \\ m_{i,k} = \displaystyle\sum_{p \in \Omega_{\boldsymbol{x}_i}} w_{pi} m_p \\ \boldsymbol{u}_{i,k} = \dfrac{1}{m_{i,k}} \displaystyle\sum_{p \in \Omega_{\boldsymbol{x}_i}} w_{pi} m_p \boldsymbol{u}_p \\ \phi_{i,k} = \dfrac{1}{m_{i,k}} \displaystyle\sum_{p \in \Omega_{\boldsymbol{x}_i}} w_{pi} m_p \phi_p \end{pmatrix} \quad \rightarrow \quad \begin{pmatrix} n_k \\ m_k \\ m_k \boldsymbol{u}_k \\ m_k \phi_k \end{pmatrix} (t + \Delta t, \boldsymbol{x}_i), \tag{3.5}$$

which involves parcels with $\boldsymbol{x}_p(t + \Delta t)$ in the $\Omega_{\boldsymbol{x}_i}$ ensembles to be associated to the relevant $\boldsymbol{x}_i$.

The full sequence including transport and splitting reads as follows:

1a) Scatter is done according to the mapping of Eq. (3.4).
1b) Transport: $\boldsymbol{x}_p(t + \Delta t) = \boldsymbol{x}_p(t) + \boldsymbol{u}_p(t) \Delta t$. These N_p trivial linear extrapolations exactly solve the transport part of the kinetic equation in the context of operator splitting.
2a) Gather (projection) according to the mapping of Eq. (3.5).

2b) Coupling (phase space evolution): Due to the above operator splitting, the remaining operators of Eq. (2.4) have to be solved. These operators sum up to coupling, which is detailed in Eq. (3.1). The Eulerian fields encounter a phase space evolution (due to drag, heating, evaporation, break-up, collisions) on Δt. At the end of this step, the Eulerian field is the approximated solution of Eq. (2.4) at time $t_0 + \Delta t$. This splitting is a first order Lie splitting [22].

A key attribute of this formulation is the ability to transform an instantaneous Lagrangian description (point-wise masses at arbitrary locations after step 2a) into an Eulerian description (fixed locations). To accomplish this, a conservative projection is performed on the $2^{n_{dim}}$ closest neighbors, where n_{dim} is the physical space dimension. The projection only needs the knowledge of the parcels and cell centers positions and is performed independently for each parcel. The weights are based on the Cartesian-projected distances of the parcel to the cell centers. An Eulerian node $\boldsymbol{x}_i = (x_i, y_i, z_i)$ receives mass from parcel p under the condition that parcels in immediately neighboring cells contribute to a cell, that is, as long as they are not located beyond the center of the neighbors. The repartition is done using a weight function w_{pi}, which is defined to have the following properties:

- Isotropy: The weight w_{pi} is direction-independent so 1D-weights $w_{pi} = \prod_{\alpha \in x,y,z} w_{pi,\alpha}$ can be defined.
- Linearity: The 1D-weights $w_{pi,x}$ depend only and linearly on the normalized distance to the cell center $\eta_x = \frac{x_p - x_i}{x_{i\pm1} - x_i}$.
- Convexity: For particles in cell x_i, the nearest neighbor $x_i \pm 1$ guarantees that $\eta_x \in [0, 1]$.
- Consistency: The mass goes completely to x_i if x_p matches x_i so that $w_{pi,x} = 1$ if $\eta_x = 0$.
- Conservativity: The weight is symmetric; i.e., $w_{pi,x}(1 - \eta_x) = 1 - w_{pi,x}(\eta_x)$.

A particular property resulting from the last criterion is that the mass fully goes to $x_i \pm 1$ if x_p matches $x_i \pm 1$ so that $w_{pi,x} = 1$ if $\eta_x = 0$. We finally choose the normalized distance to the neighboring cells' centers, which is the only linear choice,

$$w_{pi,x} = 1 - \eta_x, \quad w_{pi,y} = 1 - \eta_y, \quad w_{pi,z} = 1 - \eta_z, \tag{3.6}$$

where the definition of η_x is based on wether x_p is closer to x_{i-1} or x_{i+1} as said previously (convexity). We call this Eulerian approach with forward semi-Lagrangian transport scheme and linear projection FSL-LP.

Step 1a) can be renewed in a cycle shown in Fig. 3.2, defining the Lagrangian state at $t + \Delta t$. Therefore the splitting sequence can be summarized using symbolic operator notations:

$$\boldsymbol{U}(t + \Delta t) = \mathscr{C} \prod_{k=1}^{N_{\text{sec}}} (\mathscr{T}_k) \;\; \mathscr{T}_g \;\; \boldsymbol{U}(t) \quad \text{with} \quad \boldsymbol{U}(t) = \begin{pmatrix} \rho_g \\ \rho_g \boldsymbol{u}_g \\ \rho_g e_g \\ n_k \\ m_k \\ m_k \boldsymbol{u}_k \\ m_k T_k \end{pmatrix} (t). \tag{3.7}$$

The key is to perform frequent projections of the mass and momentum on an Eulerian mesh in order to use the Eulerian fields for the coupling step (Euler-Euler coupling), and redefine the way the field is sampled by Lagrangian parcels (the projection/emission of Lagrangian parcels can be seen as a remeshing). Since all the passive scalars are projected using convex combinations with linear, geometrically defined, positive coefficients, realizability is guaranteed whatever the moments. Finally, the cost in the Multi-Fluid context is known: the assumption of size-conditioned velocities allows to use only one parcel per location and per section so we have a $N_p = N_{\text{cell}} \times N_{\text{sec}}$ procedure, as used in vortex methods [48, 14].

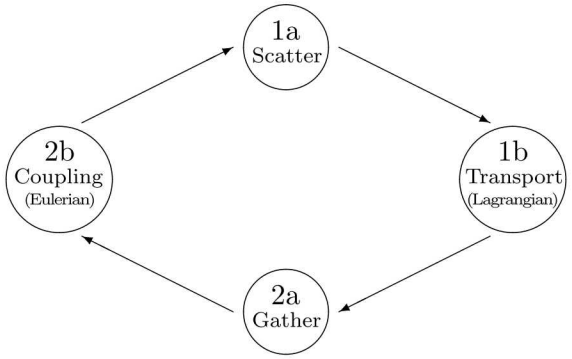

Figure 3.2. Schematic of the gather-scatter cycle as the algorithm for the FSL transport scheme.

3.2 Accuracy of the method

3.2.1 Theoretical arguments

The space-time order of semi-Lagrangian methods is of the form [6, 55, 32]

$$|\text{SL error}| < C_1 \Delta t^p + C_2 \frac{\Delta x^{r+1}}{\Delta t}. \tag{3.8}$$

In the specific case of a Verlet time integration, Respaud and Sonnendrücker [55] prove the L^1 convergence of the method and an error $O(\Delta t^2) + O(\Delta x^2) + O(\frac{\Delta x^2}{\Delta t})$. This expression provides a guidance on what can be expected in our case. The first part of the error is introduced by the characteristic reconstruction, which is exact in our case so that $C_1 = 0$. The second part is introduced by the projection scheme, whose space accuracy is of order 2 in our case as demonstrated later, so that $r = 1$. Thus, for a fixed time step, we expect a rate of convergence of order 2 with the cell size.

The characteristic that is enforced during the transport step is exactly that of the initial kinetic equation Eq. (2.1) and describes free streaming. Conversely, as soon as a non-linearity (particle crossing) arises, this characteristic does not belong to the PGD problem: if crossing occurs within a time step, velocity-averaging is not correctly reproduced by the transport step of the semi-Lagrangian approach. The PGD treatment of trajectory crossings, however, is recovered at the projection step, i.e., the particles with multivariate velocities are averaged into a "monokinetic"

cloud. Therefore resorting to large CFL numbers, though not a threat to stability *per se*, increases the risk of discrepancies to the exact PGD solution. An analytical formula for the evolution of a Dirac δ-function of density under successive projections is derived in the following Section. The considerations above confirm that the method introduces an error of order 2, which is diffusive and dependent on the CFL number. This study also illustrates the unconditional stability of the approach, allowing CFL numbers larger than 1.

The method's order can be increased by considering higher order projections, involving larger stencils [51, 16, 14]. The coefficients then stem from the choice of a projection kernel, as extensively discussed by Cottet et al. [14]. These authors show the efficiency of a dimensional splitting of the projection step by reducing the problem to the choice of a proper 1D kernel based on compacity and smoothness arguments. The important question is then how to cope with oscillatory behavior in under-resolved and discontinuous regions. Preserving realizability and in particular positivity is of paramount importance in our fully-coupled spray problem, whereas higher-order demonstrations have been made for the transport of passive (one-way coupled) scalars [14]. The path is to perform a limitation of the reconstructed values [5] when local gradients are strong. Moreover, in the case of moment methods, the gradients of all the moments have to be examined; i.e., the projection should depend on the other particles' mass, momentum, and higher order moments. But this step has to be done in a conservative and positivity-preserving fashion. For the moment, we will only consider the low-order formulation for the sake of good mass conservation properties and robustness, with the caveat that the numerical diffusion of the linear projection might be impractical for some problems.

3.2.2 Analytical study of 1D-cartesian advection

The error of the FSL scheme can be studied analytically when using the linear projection operation. The analysis can be focused to the advection of a single parcel (a Dirac δ-distribution) because any spatial profile can be retrieved by superposition (linearity of transport) when no trajectory crossing occurs. For the sake of simplicity, we hereafter assume that the grid is uniform and 1D with a characteristic length Δx. Also, the parcel initially coincides with a cell center $x_p(0) = 0$, and it moves at constant velocity u. Thus the CFL number is defined as $c = \frac{u\Delta t}{\Delta x}$. We describe the problem in dimensionless form so that $m_p = 1$. After the first advection step ($t_1 = \Delta t$), the parcel is located at $x_p(t_1)/\Delta x = c$.

The projection step involves sharing the mass between the two neighbors, which are $x_{\lfloor c \rfloor} = \lfloor c \rfloor$ and $x_{\lceil c \rceil} = \lceil c \rceil$ if $\lfloor \cdot \rfloor$ and $\lceil \cdot \rceil$ are the floor and ceiling functions respectively. Note that the indices match the values due to non-dimensionalization and to the fact that $\lceil c \rceil = \lfloor c \rfloor + 1$. The two neighbors respectively receive

$$m_{\lfloor c \rfloor} = w_{\lfloor c \rfloor}(\eta_{\lfloor c \rfloor}) = 1 - \eta_x = 1 - \frac{x_p(t_1) - x_{\lfloor c \rfloor}}{x_{\lceil c \rceil} - x_{\lfloor c \rfloor}} = 1 - \{c\}$$

$$m_{\lceil c \rceil} = w_{\lfloor c \rfloor + 1}(\eta_{\lfloor c \rfloor + 1}) = 1 - w_{\lfloor c \rfloor}(\eta_{\lfloor c \rfloor}) = \{c\},$$

where the notation for the weights has been simplified from $w_{pi,x}$ to w_i and where $\{\cdot\} \in [0, 1]$ is the fractional part. This complies with all the weight requirements defined in Section **??**. Meanwhile, the other grid points receive nothing; i.e., $m_i = 0$, $i \neq \{\lfloor c \rfloor, \lceil c \rceil\}$ so that mass is conserved; i.e., $\sum m_i = (1 - \{c\}) + \{c\} = 1$. The next transport step brings the two non-void parcels p and p' to

be located at

$$\begin{array}{l} x_p(t_2) = x_{\lfloor c \rfloor} + c = \lfloor c \rfloor + c \\ x_{p'}(t_2) = x_{\lceil c \rceil} + c = \lceil c \rceil + c \end{array} \quad \text{and projected on} \quad \begin{array}{c} (x_{\lfloor 2c \rfloor}, x_{\lfloor 2c \rfloor + 1}) \\ (x_{\lfloor 2c \rfloor + 1}, x_{\lfloor 2c \rfloor + 2}) \end{array}$$

so that the three grid points now involved with receiving mass are $x_{\lfloor 2c-1 \rfloor}$, $x_{\lfloor 2c \rfloor}$, and $x_{\lfloor 2c+1 \rfloor}$ with

$$\begin{aligned} m_{\lfloor 2c-1 \rfloor} &= \{c\}^2 \\ m_{\lfloor 2c \rfloor} &= 2\{c\}(1-\{c\}) \\ m_{\lfloor 2c+1 \rfloor} &= (1-\{c\})^2, \end{aligned}$$

with the middle point receiving two contributions. This scheme exactly replicates Pascal's triangle such that the Eulerian masses can be deduced at each time step using a basic recursion. Because the problem is invariant by translation, we can now take the notation m_i^n at time step n, where i is a translated space index so that $m_i^n = 0$ for i outside of $[\![0, n]\!]$. The fractional part of the CFL is now simply noted c, keeping in mind that the overall method is perfectly valid for $c > 1$ but boils down to the result with $c' = c - \lfloor c \rfloor \in [0, 1[$ plus a translation of $n\lfloor c \rfloor$ grid points. We can finally solve the problem at every grid point i and every time step n using the binomial monoms

$$m_i^n = \binom{n}{i} c^n (1-c)^{n-i} \quad \text{with} \quad \binom{n}{i} = \frac{n(n-1)\cdots(n-i+1)}{i(i-1)\cdots 1}.$$

Mass conservation is retrieved using Newton's formula

$$\sum_{i=0}^{n} m_i^n = \big(c + (1-c)\big)^n = 1.$$

The result after several advection-projection steps is given in Fig. 3.3 in the case of CFL = 0.5. The significant diffusion of mass to the neighbor cells is clearly visible.

Using the above analytical formula, we can exactly compute the numerical error of the method. For n large enough, the binomial distribution behaves like the normal law with expectancy $\mathbb{E}(m_i^n) = nc$ and variance $\mathbb{V}(m_i^n) = nc(1-c)$. Moreover, this Gaussian distribution is the solution of an advection-diffusion equation applied to the initial Dirac δ-distribution. We refer to this equation as the so-called "modified equation" and it reads (in dimensioned form)

$$\partial_t \rho + \partial_x \rho u_{\text{num}} = D_{\text{num}} \partial_{xx} \rho \quad \text{with} \quad u_{\text{num}} = \frac{c\Delta x}{\Delta t} \quad \text{and} \quad D_{\text{num}} = \frac{1}{2}\frac{\Delta x^2}{\Delta t}\{c\}(1-\{c\}). \tag{3.9}$$

By identification, we can state that the present scheme achieves an approximation of Eq. (3.9) that is of higher order compared to the approximation of the original system given by Eq. (3.3). Therefore the numerical errors can actually be quantified from the modified equation: the scheme is exact on group velocity ($u_{\text{num}} = u$), it features diffusion ($D_{\text{num}} \geq 0$), but it is non-dispersive since no additional odd spatial derivatives are present. The modified equation also shows that the Lagrangian transport coupled to a projection operation renders the exact solution for $c \in \mathbb{N}$ (yielding $D_{\text{num}} = 0$) while diffusion error is maximum for $\{c\} = 1/2$. Numerical diffusion is expected to smear the sharpest profiles just as physical diffusion would. This effect is illustrated in Fig. 3.4 on the advection of a signal presenting a discontinuity and a continuous span of space frequencies. After 25 time steps, the highest frequencies appear to be significantly smeared out but the scheme is strictly non-oscillatory and positivity-preserving.

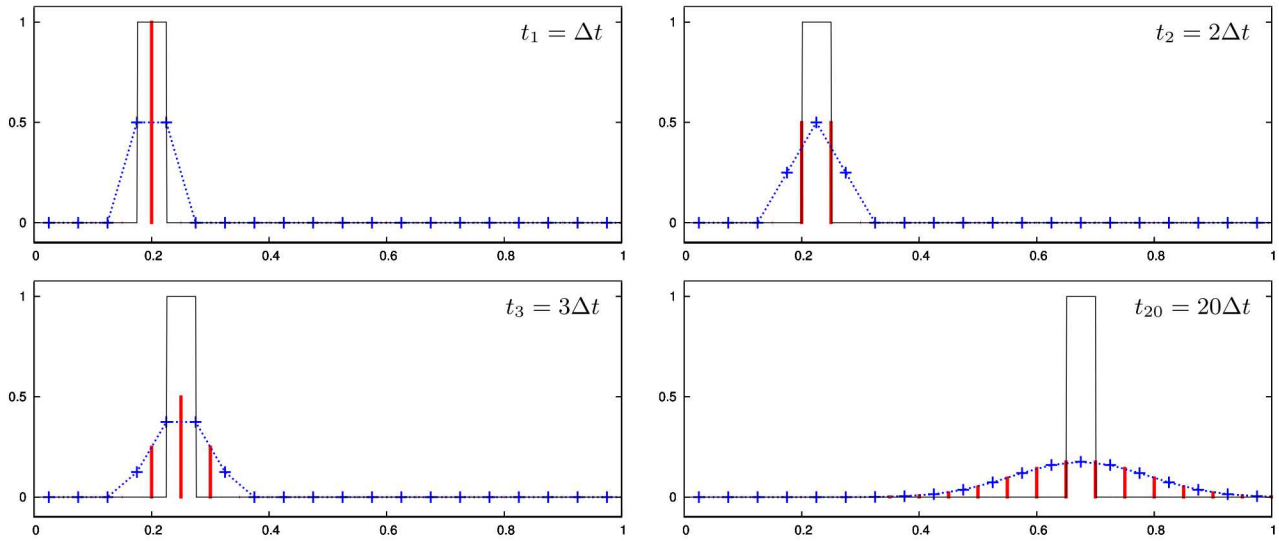

Figure 3.3. Transport of the sharpest field possibly resolved (a discretized δ-shock) using FSL-LP at CFL $c = 0.5$; **Solid line**: Exact signal; **Stick**: Parcel after transport step; $\cdots+\cdots$: Eulerian field after gather step.

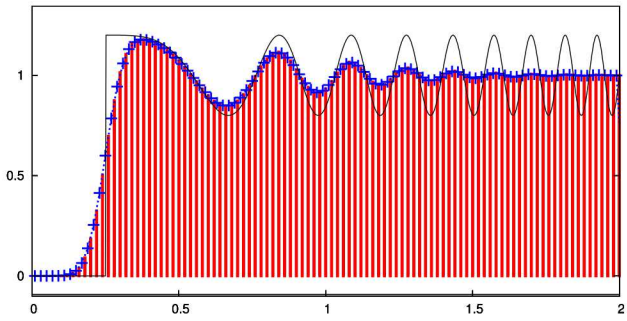

Figure 3.4. Transport of a multi-scale signal using the FSL-LP scheme at CFL $c = 0.5$ after 25 time steps; **Solid line**: Exact signal; **Stick**: Parcel after transport step; $\cdots+\cdots$: Eulerian field after gather step.

Remark: If we consider weights $w_x(\eta_x)$ that are non-linear in η_x and such that the non-linear function still enforces the above properties, especially $w_i(1-\eta_x) = 1 - w_i(\eta_x)$, the same steps can be taken by substituting $w_i(\{c\})$ to $\{c\}$ so that the instantaneous positions

$$m_i^n = \binom{n}{i} w_i(\{c\})^n \big(1 - w_i(\{c\})\big)^{n-i}$$

are obtained. It is obvious that mass is again conserved thanks to the symmetry property. However, we now have $\mathbb{E}(m_i^n) = n w_i(\{c\})$ and variance $\mathbb{V}(m_i^n) = n w_i(\{c\})(1 - w_i(\{c\}))$. This is interesting from the point of view of diffusion since we can get D'_{num} arbitrarily close to 0 for any c. Unfor-

tunately the advection velocity $u_{\text{num}} = \frac{w_i(\{c\})\Delta x}{\Delta t} = \frac{w_i(\{c\})}{c}u$ is directly affected by the non-linear process, being altered by a factor $\frac{w_i(\{c\})}{c}$. To summarize, a non-linear weighting repartition leads to either decreased phase velocity and decreased diffusion or increased phase velocity and increased diffusion. Thus diffusion error has been traded for dispersion error. The linear weights are the only possible ones to perform a non-dispersive projection when purely relying on the geometry to compute the weights.

3.3 Verification of the FSL-LP transport scheme

We now perform verifications for the FSL-LP transport scheme using 1D cartesian cases, a 2D structured case, and a 0D case with sources. This allows us to quantify the order of the method, to assess its qualities for practical cases, and to verify its constitutive modules.

3.3.1 1D linear advection

We consider the case of the advection of a smooth profile at uniform velocity. This study complements the analytical assessment of FSL-LP performed in Section 3.2.2. A Gaussian density profile is selected for its smoothness and the reference solution can be devised analytically, thanks to the linearity of advection. The goal is to assess the actual order of the FSL-LP transport scheme. A regular and a stretched mesh are considered to discretize the segment $[0, L_x]$ with $L_x = 1$. The stretched mesh is stretched towards $x > 0$ according to $x_i = L_x(i/N_x)^2$. The convergence of general semi-Lagrangian methods is a topic under study [38, 39], but, in the present case of FSL with a linear projection, this matter is dominated by the accuracy of the projection on the stretched grid. We here propose an empirical verification on a linear advection case. The error is assessed using the L^1 norm

$$E_{N_x} = \frac{1}{N_x}\sum_{i=1}^{N_x} |m_{N_x}(x_i) - m_{\text{ref}}(x_i)|.$$

Results are given in Fig. 3.5 after one time step with a fixed $u\Delta t = 1/20$ for all levels of refinement. This proves that the method is convergent regardless of the type of mesh. The slopes indicate a local error of order 2 for both types of mesh. This means that, for a fixed CFL, the global order of the method would be 1 because of the errors introduced by the number of time steps linearly increasing with N_x. Note however that the method can be used at arbitrary CFL. Note also that there exist, in the regular mesh case, some discretizations for which the error dramatically drops (here by 6 orders of magnitude). This corresponds to integer CFL numbers, for which the projection is exact. As a conclusion, the method is convergent with the expected order on both Cartesian and stretched meshes.

3.3.2 1D PGD convection with vacuum and shock formation

We now consider a case with convection; i.e., a type of transport where the velocity information is transported together with the quantity of interest (here mass) as opposed to advection where velocity is exogenous. In particular, we examine the ability of FSL-LP to deal with the full physics

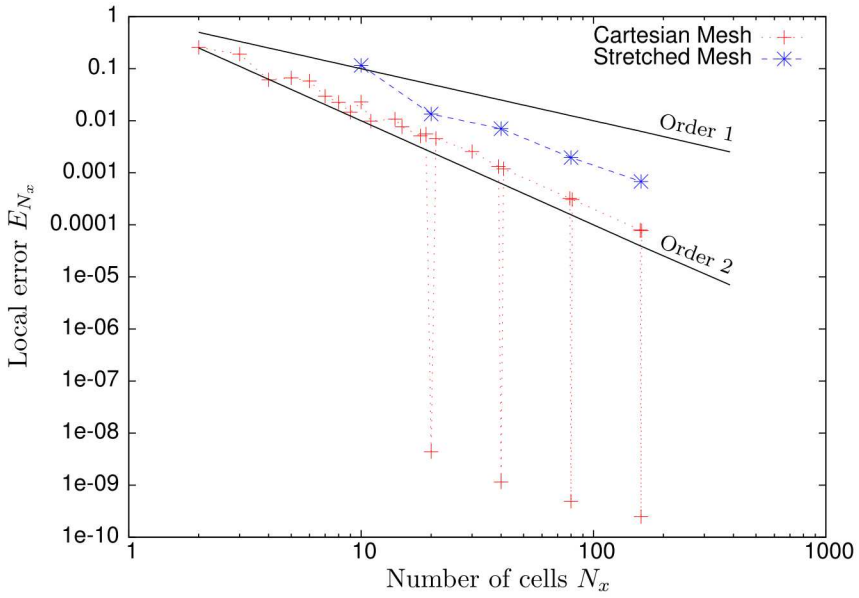

Figure 3.5. Convergence of the gather-scatter method on 1D advection of a Gaussian profile.

of PGD. To do so, we take the first test problem defined by Bouchut et al. [10]. It is a 1D problem featuring a velocity discontinuity and a velocity gradient which generates density discontinuities and vacuum. The initial conditions are

$$\rho^0(x) = 0.5, \quad u^0(x) = \begin{cases} -0.5, & x < -0.5, \\ 0.4, & -0.5 < x < 0, \\ 0.4 - x, & 0 < x < 0.8, \\ -0.4, & x > 0.8. \end{cases} \tag{3.10}$$

We compare in Fig. 3.3.2 the FSL-LP results to the analytical solution provided by the authors with their first-order Godunov and kinetic schemes. The velocity field is accurately rendered and the density field appears slightly less smoothed out at discontinuities compared to the results in Bouchut et al. [10] (not shown here), but the same spike at the zero-velocity (sonic) point analyzed by Bouchut [9] is present. Finally, the $\rho = 1$ plateau is underestimated for mass conservation reasons, the missing mass being accumulated in the spike, as observed in the reference computation. Overall, our conclusion is that the FSL-LP transport scheme is fit to describe PSD. To be used for more complex spray applications, the method must now be checked for robustness and accuracy in two-way coupling.

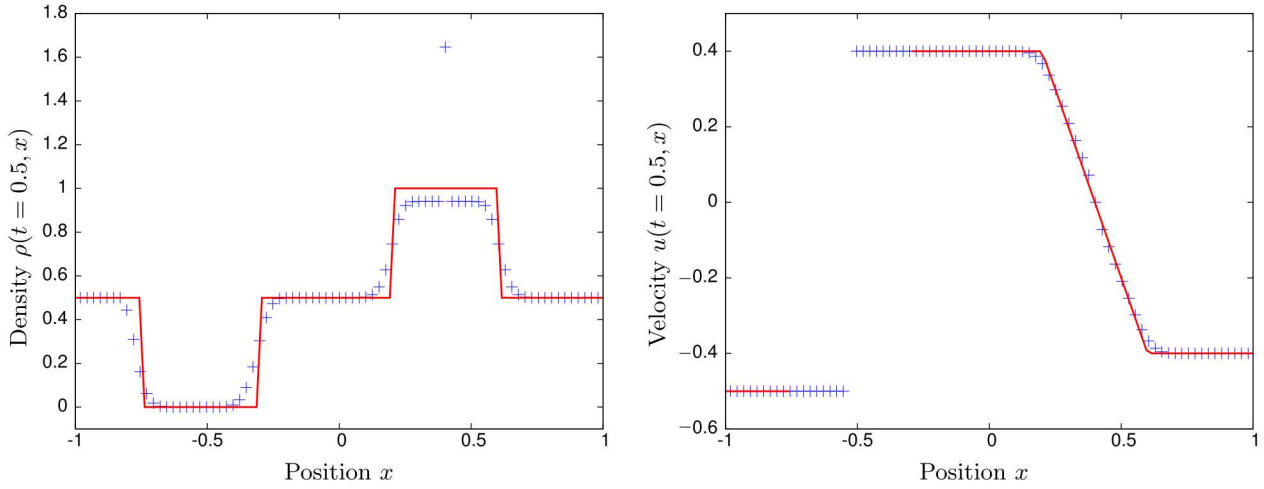

Figure 3.6. Solution at $t = 0.5$ of Bouchut et al.'s "numerical test I". Exact solution (line) and FSL-LP scheme with $\Delta x = 0.025$ and $\Delta t/\Delta x = 5/3$ (+).

Chapter 4

Strategy for LES modeling of fuel injection

4.1 Phase space integrator verification

To time-integrate the coupling operator $\mathscr{C}$, we use an explicit, Runge-Kutta 4 (RK4) scheme. We perform a quantitative verification of the two-way coupling solver based on the characteristic time and equilibrium velocity of a 0D monodisperse spray. Results are shown for various droplet sizes r_k in Fig. 4.1 (left) and for various droplet loadings in Fig. 4.1 (right). The reference times and equilibrium velocities are computed from the following analytical formulae

$$\tau_c^{\boldsymbol{u}} = \frac{\tau^{\boldsymbol{u}}(r_k)}{1 + m_k/\rho_g} \quad \text{and} \quad \boldsymbol{u}_{\text{eq}} = \frac{\rho_g \boldsymbol{u}_g + m_k \boldsymbol{u}_k}{\rho_g + m_k}$$

and the numerical results compare well. The verification of the heat exchange terms is not presented here but the terms are coded similarly. The verification of the evaporation terms is not presented. The integration module computes all three sources simultaneously, in the same RK4 sequence, therefore achieving a full coupling of the phase space.

4.2 Timescale of dense spray coupling

A local characteristic drag time, as introduced in Section 4.1, stems from eigenvalue analysis of the two-way coupled momentum equations

$$\tau_c^{\boldsymbol{u}}(t, \boldsymbol{x}) = \frac{\tau^{\boldsymbol{u}}(r_k(t, \boldsymbol{x}))}{1 + m_k(t, \boldsymbol{x})/\rho_g(t, \boldsymbol{x})} \tag{4.1}$$

where $\tau^{\boldsymbol{u}}(r)$ is the characteristic time of the drag force $\mathbf{F}$ and the local drop radius r_k can be computed from n_k and m_k. The equation shows that the characteristic time for the two-way coupled system becomes shorter with increasing liquid loading; and the coupling does actually maintain the velocities and temperatures close to equilibrium, provided that the corresponding characteristic timescales will be small. The same argument applies to a coupled heat transfer time τ_c^T by using $\tau^T(r)$ the characteristic time of H. The corollary of these observations is that the discrepancy introduced by using simple spherical closures for drag and evaporation, where spray structures may be in fact far from spherical, does not have a significant impact in regions where the overall dynamics of the spray is dominated by the liquid phase.

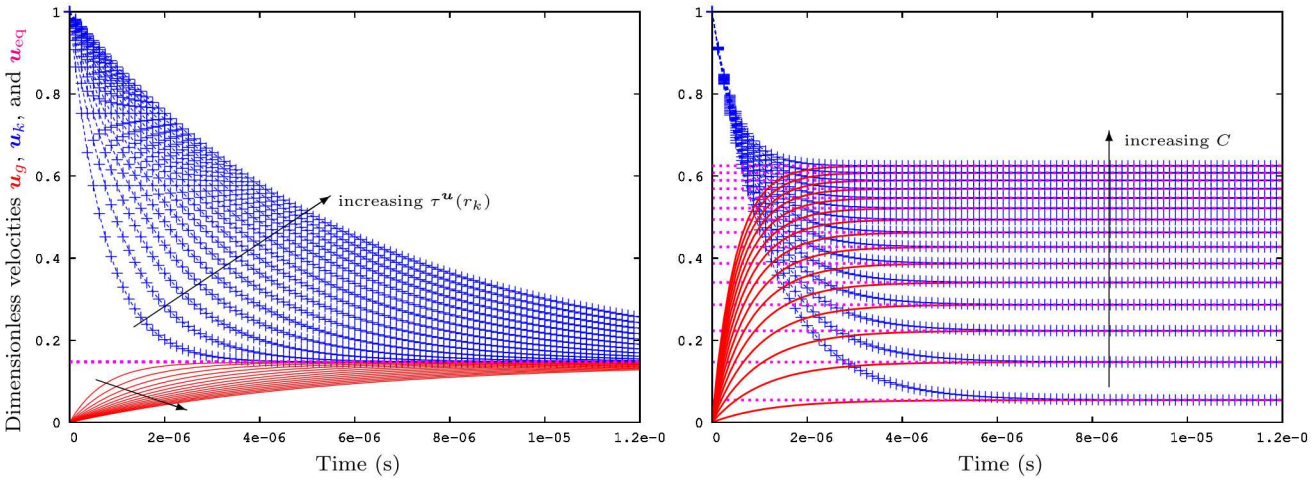

Figure 4.1. Computations of drag with two-way coupling (0D) giving quantitative verification of the phase space integrator – Left: Various droplet sizes/characteristic times with $C = 0.17$; Right: Various mass loadings with $\tau_c^{\boldsymbol{u}} = 10^{-6}\,\mathrm{s}$ – Solid: $\boldsymbol{u}_g$; $-+-$: $\boldsymbol{u}_k$; $\cdots$: $\boldsymbol{u}_{\mathrm{eq}}$.

4.3 Verification of near-nozzle multiphase flow

A set of calculations are performed on a simplified case of direct fuel injection (spray A conditions, extensively described in Chapter 5) with both the Multi-Fluid FSL-LP scheme and the Coupled Level-Set Volume of Fluid (CLSVOF) approach [41, 1]. The comparison is conducted at an early stage of injection, namely when the liquid trajectory is still weakly influenced by the surrounding gas. We choose to look at an instant $3.7\,\mu$s after the start of injection (ASOI) with a simple plug flow as a model boundary condition for the liquid; i.e., a laminar profile with no boundary layer. Results are given in Fig. 4.2. Strong entrainment is created in the chamber because the liquid mass fraction and momentum ratio are high. The two approaches agree very well on the gas flow field and on the inertial behavior of the liquid core. The penetration lengths match to within 1%. The difference in the jet tip morphology is due to the lack of surface tension model in the Eulerian Multi-Fluid calculation.

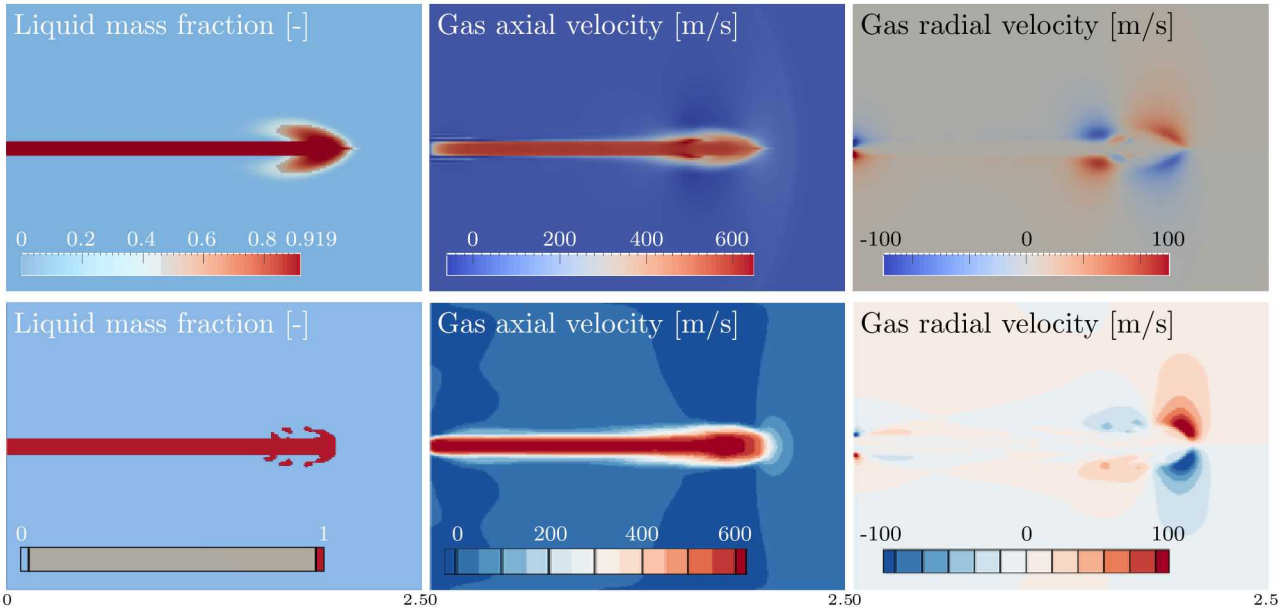

Figure 4.2. Multi-Fluid (top) and CLSVOF (bottom) injection with a laminar boundary condition at 3.7 μs ASOI (center plane slices) – Lengths are in mm.

Chapter 5

Spray A demonstration

In this final chapter the target application is developed: a realistic DNS of fuel injection coupled to the LES of the resulting spray flame. Recalling the schematics of 1.1, details of the CLSVOF simulation to include flow internal to the injector and the primary atomization of the liquid jet are presented in the first part. The second part builds on intermediate cases of monodisperse non-evaporating and evaporating sprays in RAPTOR, see Table 5.1, to arrive to the final demonstration. The configuration of choice, spray A, has been extensively studied and we refer the reader to Bardi et al. [4] and subsequent publications for more details.

	Near-nozzle monodisperse	Polydisperse reacting
Liquid density	$\rho_l = 702\,\mathrm{kg/m^3}$	$702\,\mathrm{kg/m^3}$
Liquid temperature	$T_l = 363\,\mathrm{K}$	$363\,\mathrm{K}$
Chamber pressure	$p_g = 60/80\,\mathrm{bar}$	$60\,\mathrm{bar}$
Chamber temperature	$T_g = 900/1200\,\mathrm{K}$	$900\,\mathrm{K}$
Gas composition	N_2	Preheating residuals
Gas density	$\rho_g = 22.4\,\mathrm{kg/m^3}$	$22.8\,\mathrm{kg/m^3}$
Gas viscosity	$\mu_g = 4.32 \times 10^{-5}\,\mathrm{Pa.s}$	$4.32 \times 10^{-5}\,\mathrm{Pa.s}$
Nozzle diameter	$d = 90\,\mu\mathrm{m}$	$90\,\mu\mathrm{m}$
Inlet velocity	$\boldsymbol{u}_k(t, \boldsymbol{x}_0) = U_l = 600\,\mathrm{m/s}$	$600\,\mathrm{m/s}$
Jet Reynolds number	$\mathrm{Re}_g = \frac{\rho_g U_l d}{\mu_g} = 28\,000$	$28\,000$
Initial droplet radius	$r_p = 2\,\mu\mathrm{m}$	see Table 5.2
Drag characteristic time	$\tau^{\boldsymbol{u}} = \frac{\rho_l r_p^2}{18\mu_g} = 14.4 \times 10^{-6}\,\mathrm{s}$	multiple times
Domain size	$L_x \times L_y \times L_z = 9.6 \times 3.2 \times 3.2\,\mathrm{mm^3}$	$54 \times 10.8 \times 10.8\,\mathrm{mm^3}$
Mesh	$N_x \times N_y \times N_z = 768 \times 256 \times 256$	$1200 \times 240 \times 240$
Time step	$\Delta t = 0.008\,\mu\mathrm{s}$	$0.040\,\mu\mathrm{s}$
Wall clock time@1600 CPUs	WCT $< 1\,\mathrm{day}$	$6\,\mathrm{days}$

Table 5.1. Characteristics of the Spray A computations.

5.1 DNS (via CLSVOF) of Spray A near field

The CLSVOF simulation included the tip of the injector and was carried out for a specific injector from Robert Bosch LLC (part of the Spray A batch, specimen 210675): the model tip of the nozzle was reconstructed based on radiographic tomography data of the hardware. The time-dependent opening needle motion, including wobble, was also implemented in order to minimize the sources

of discrepancy between lab measurements and simulations. The simulation covered the first 365 μs from needle activation, of which the last 25 μs follow the appearance of the liquid from the orifice exit (apparent start of injection, or ASOI) and its atomization. While long by DNS standards, this time interval still does not include the complete injection transient: steady-state penetration of the liquid jet in the injection cycle of Spray A occurs approximately after 40 μs from ASOI.

The injector representation required a surface mesh (triangular tessellation) of the internal and external walls as well as of the needle: the smallest edge length of this mesh was of $1 - 2$ μm at the orifice exit. The injector was separated in its two components shown in Fig. 5.1: the cap, or tip of the injector, fixed; and the needle (in green), allowed to move. The sac is the region enclosed between the cap and the needle. The base grid containing the injector was a regular Cartesian $64 \times 64 \times 576$ box with the longest side, oriented along the injector's axis, of length 1.53 cm (170 times the exit orifice diameter). This length was substantially longer than in similar high-fidelity simulations because we intended to follow the jet penetration for a sufficient time period. Three levels of refinement were added to the coarse level in order to obtain a minimum grid spacing of 3.32 μm, corresponding to 27 computational cells across the orifice diameter. At this grid resolution, the stable time step for the flow of interest (with a supersonic transient in the gas phase) was of the order of three nanoseconds. With adiabatic wall conditions for the injector, this simulation is referred in the following with the label AB. A fourth level of refinement was added in order to verify grid convergence in the early stage of injection, bringing the cell count to more than 400M cells (AB4 simulation).

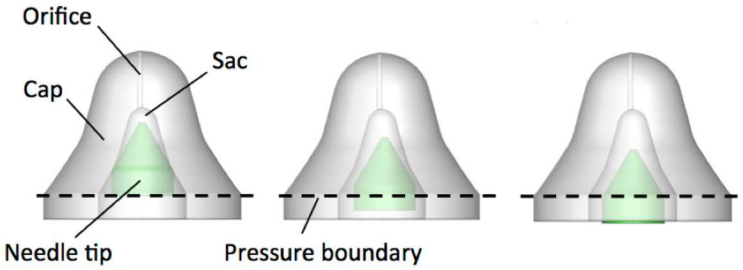

Figure 5.1. Computational set-up for moving geometry in CLSVOF.

The needle velocity was calculated by differentiation of the displacement values read from the trajectory file, while the fixed injection pressure of 150 MPa was applied directly at the boundary face (dashed line in Fig. 5.1). A fixed exit pressure of 2 MPa was applied to the other five sides of the computational domain box, assuming an open vessel. The velocity field at the six sides of the computational box was set by extrapolation. The initial temperature of the fuel was uniformly set to 343 K in both the reservoir and the cap. The initial temperature of the gas was set to 303 K. The 303 K temperature corresponds to the chamber non-evaporating condition used for radiographic measurements of fuel mass at the Argonne National Laboratory (ANL). In the following, the main simulation results from [2] are summarized.

Calculations were carried out on the Redsky Sandia cluster by using 128 SUN X6275 blades (2.93 GHz dual socket/quad core configuration with 12 GB RAM per blade) for a total of 512 cores.

This is only an average figure, because in this AMR simulation the computational cost increased with the development of the spray outside of the injector. At the beginning of injection, the region of the computational domain occupied by the liquid phase was confined to the sac, but eventually the solution-adaptive mesh refinement algorithm added several more computational grid boxes to continue capturing the liquid surface. Starting with approximately 70 millions cells, their count later surpassed 250 millions; in the latest stages of the simulation, more than 256 blades, or 1024 cores, were necessary.

At the onset of needle lifting, we observed that a small amount of gas was ingested in the injector's sac due to the interference between needle tip and injector walls. Most of the gas was then ejected in an under-expanded jet outside of the orifice. The fuel temperature at the orifice exit during the opening transient remained within 15 Kelvin from the prescribed reservoir temperature with adiabatic wall conditions. As the needle became fully unseated, the remaining viscous effects concentrated at the orifice inlet and the exit temperature reached a constant value; the exit fuel density correspondingly decreased from 790 kg/m^3 upstream of the needle gap to 711 kg/m^3 at the exit of the injector.

The penetration of the uninterrupted core of the jet was found to be consistent with sample-averaged X-radiography measurements of the trajectory of the tip at cold gas conditions. Conversely, jet break-up length, which was identified from the sudden shortening of the uninterrupted liquid core, depended on the injector's wall boundary conditions: it occurred within 7 mm from the orifice for the adiabatic wall case and within 6 mm for the isothermal case. This difference was attributed to the dependence of the surface tension coefficient on temperature.

In the process of jet breakup, a few large chunks of liquid (larger than than the orifice diameter) separated from the core while a broad variety of smaller drops was also detected. Drops in the same intermediate-to-large equivalent diameter range were examined with respect to their shape, which was taken as an indicator of whether they could further fragment before equilibrating with the surrounding gas flow. Approximately two thirds of the sample population were found to possess a shape sufficiently close to spherical, while the remaining third had a more elongated shape (ligaments) and could undergo secondary breakup. The shape of the tip of the jet was far from the regular shape that is often assumed as the initial condition of injection simulations (say, a cylinder terminated by a half sphere). Eventually however, the peeling of ligaments from the jet core in the interaction with the gas flow caused a tip shape similar to a mushroom head; this sequence is rendered in Figure 5.2, where the top panel shows the jet tip in a reference frame moving with it.

The distribution of liquid drops that formed directly from the jet was assessed by the following post-processing procedure. For a given snapshot of the solution, the zero iso-surface of the liquid-gas level set was extracted and reduced to a tessellation made of triangular or quadrilateral faces. A simple procedure then separated from each other structures that did not have nodes in common, generating polyhedra that corresponded each to a distinct liquid shape. The number of faces of a polyhedron could vary from several thousands to a few tens. From them, surface and volume were calculated. The volume calculation was carried out by subdividing each polyhedron in tetrahedra or pyramids, whose base is one the faces and whose vertex is a reference point (the center of mass of all the nodes in the shape, for instance). Finally, the diameter of of equivalent-volume sphere, $D_V = (6V/\pi)^{1/3}$, was evaluated, with V the volume of the individual drop.

To assess the convergence of the resulting spray distribution, the snapshot at 6 μs of the four-level refinement AB4 simulation was processed and compared with the distribution from AB at the

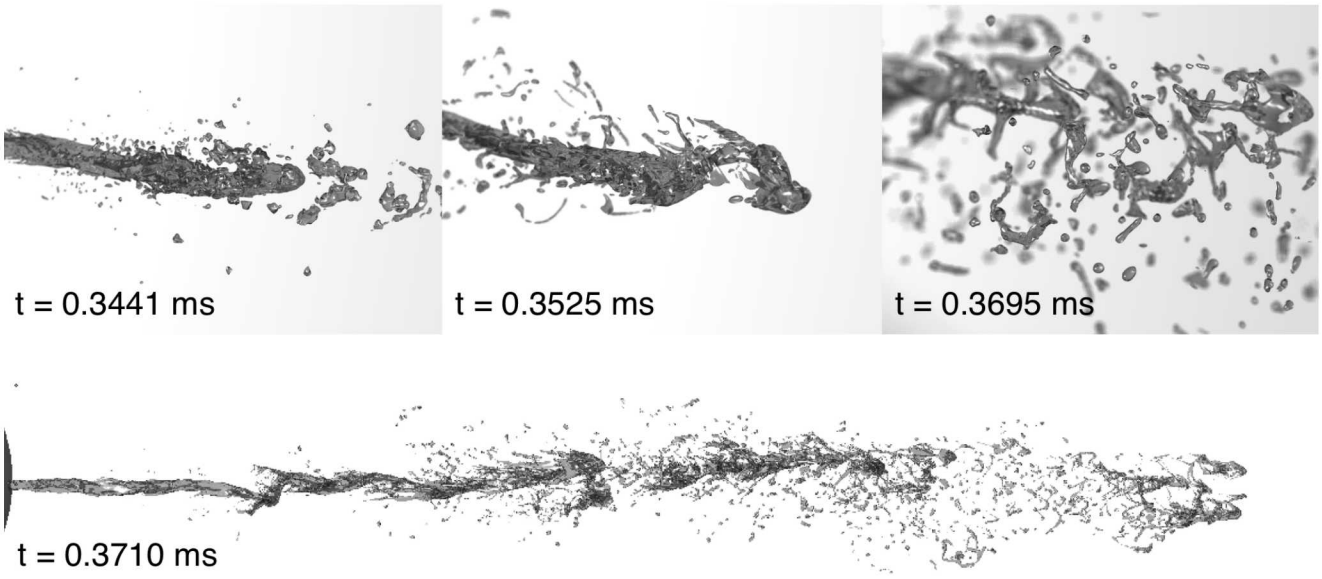

Figure 5.2. Ray-tracing rendering of the fuel jet outside of the injector. Top: the jet tip at three consecutive time snapshots. Bottom: the full length of the jet outside of the injector.

same point in time. In both snapshots the incipient spray appeared to be mostly formed by ligaments. Even though an equivalent diameter alone would be insufficient for describing their shape, the two distribution plots for D_V are shown in 5.3. In comparing the two diagrams, we assume that droplets with equivalent diameter below $2\Delta x$ are not sufficiently supported by the grid resolution and need to be discarded (but methods exist to transfer their representation to Lagrangian particles, see [40]). With 145 remaining samples for $\Delta x = 3.32$ μm and 269 for $\Delta x = 1.66$ μm, we see that the latter distribution is slightly skewed toward larger droplets (each histogram is normalized by the total number of the samples). The direct comparison of the two simulation snapshots reveals that some intact ligaments in the four-level simulation appear to have already undergone breakup in three-level grid. The spurious breakup of a liquid surface is a well-known signature of insufficient grid resolution: but a previous study [3] has shown that an interface-capturing technique similar to the one used here eventually yields to a converging spray size distribution, which in turn approached the measured distribution, under sufficient grid refinement. Thus, for the current study we can assume that only the intermediate-to-large size droplet population is converged, while acknowledging that the majority of droplets observed in the actual experiment is actually left out from the baseline simulation.

An example of D_V distribution is shown in Figure 5.4 for the AB case at $t = 25.6$ μs from the start of apparent injection. At this time, 32,938 distinct liquid structures were found. Of these, 23,785 had equivalent diameter between $2\Delta x$ and 90 μs; larger liquid structures, detached from the jet core but not yet fully atomized, are not shown in the scale of the plot. The Sauter Mean

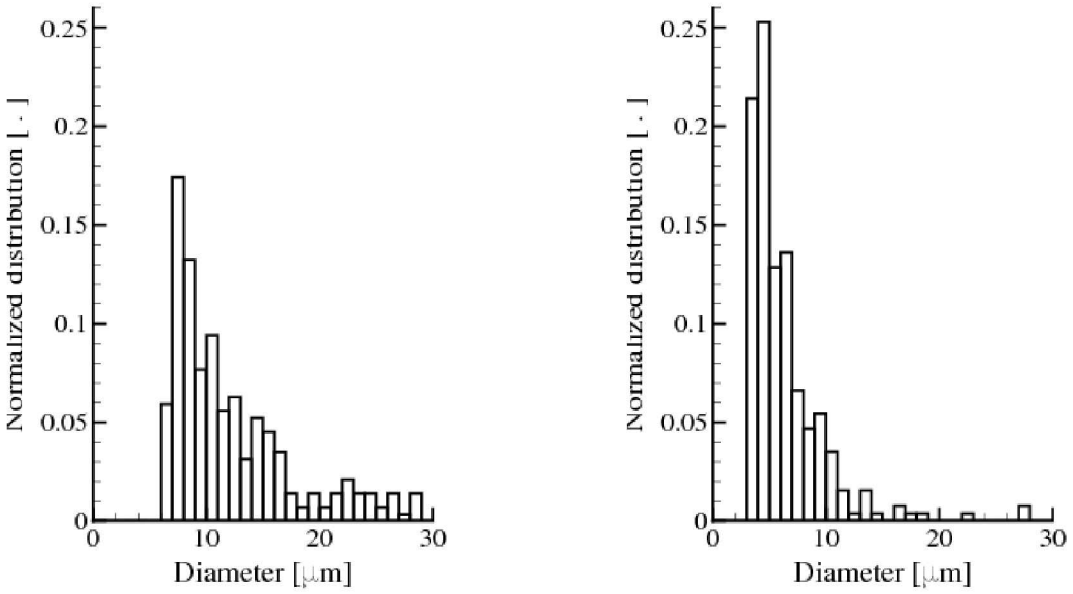

Figure 5.3. Equivalent diameter distribution at the beginning of injection ($t = 6$ μs) from $2\Delta x$ to 40 $\Delta\mu$m. Left panel: $\Delta x = 1.66$ μm; Right panel: $\Delta x = 3.32$ μm.

Diameter, SMD $= \sum D_V^3 / \sum D_V^2$, conditioned to the range 6.64 μm $< D_V <$ 90 μm, was 14.5 μm. The lognormal fit of this distribution (with parameters $\mu_{LN} = 1.9608$ μm and $\sigma_{LN} = 0.4495$ μm) was used to define the sectional discretization parameters of the polydisperse EMF spray, see Table 5.2. As the primary atomization proceeds, however, it can be expected the parameters above to vary, possibly in a downward trend.

The confirmation of these results by experimental data is at the moment limited, also because few direct measurements of droplet size distribution are available for spray A. The existing measurements show some dispersion, although the statistical size values are always smaller than the CLSVOF results. For a single-orifice Diesel injector similar to Spray A, Powell et al. [54] used Ultra-Small Angle X-ray Scattering (USA-XS), under the assumption of spherical, randomly oriented particles, to evaluate the Sauter Mean Diameter (SMD) as a function of axial distance: they found SMD ≈ 3.2 μm at a location 4 mm downstream of the orifice exit. At 900 K gas temperature, SMD was even smaller, according to preliminary results presented by the same group at the fourth ECN workshop in 2015. An alternative to USA-XS is the microscopic imaging technique by Crua et al. [17]. In the optically thin region at the edge of the spray cone where Crua's technique was used, the droplets SMD was much larger, in the range between 5 and 8 μm according to the very preliminary results also presented at the fourth ECN workshop in 2015. Currently spray size measurements cannot be extended to the core of the spray.

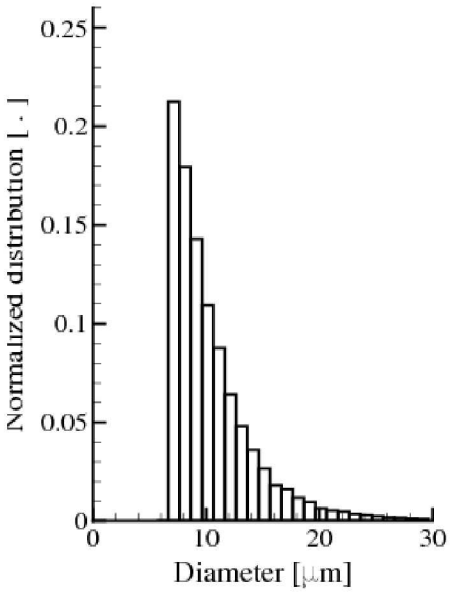

Figure 5.4. Equivalent diameter distribution at the beginning of injection

5.2 LES (via Raptor) of Spray A flame

5.2.1 Near-nozzle, non-reacting monodisperse spray

In the non-reacting version of spray A, a hot pressurized chamber is filled with pure nitrogen (N_2, $T_g = 900\,\mathrm{K}$, $P_g = 60\,\mathrm{bar}$, $\rho_g = 22.4\,\mathrm{kg/m^3}$). The fuel is injected as a round jet of liquid drops at $600\,m/s$, close to gas sonic speed, from the orifice exit. A laminar plug-flow profile is used as inlet boundary condition of the fuel jet; this simplification introduces a discrepancy with respect to the measured spray angle but does not interfere with the feasibility demonstration. This first simulation is not coupled to the CLSVOF: the droplet population is monodisperse and the prescribed diameter is small in order to test the overall quality of the numerical strategy in the presence of stiff transfer terms and strong coupling. The inlet density and temperature of the liquid phase are also fixed: $\rho_l = 702\,\mathrm{kg/m^3}$, $T_l = 363\,\mathrm{K}$. The geometry is a rectangular box of dimensions $9.6 \times 3.2 \times 3.2\,\mathrm{mm}$, which is shorter than the typical length of the steady state spray as the study is focused on the near-nozzle region of the jet. The Cartesian mesh used by Raptor is of $768 \times 256 \times 256$ cells, which translates to 7 cells per orifice diameter. The drop radius is $r = 2\,\mu\mathrm{m}$, which leads to coupling times that are close to or above the computational time step Δt. The latter is constrained by the CFL criterion based on the characteristic time of the fastest wave τ_g, which yields $\Delta t = 8\,\mathrm{ns}$.

The transfers between the two phases are computed from the resolved quantities and no dedicated two-phase LES model is used, as discussed in Section 2.2.1: It is assumed that the droplet

transport is not directly influenced by the gas subgrid turbulence and that the gas is not influenced by the droplets' subgrid motion (subgrid turbulent dispersion can be expected to play a role, but in this dense spray context no satisfactory model currently exists).

5.2.2 Case with $T_g = 900\,\mathbf{K}$

Results are shown in Fig. 5.5 for two cases where evaporation is turned off and on respectively. The high mass loading ratio, $C = \rho_l/\rho_g = 31$, at the orifice inlet demonstrates the remarkable robustness of the coupling between the two phases enabled by the FSL-LP scheme. The mass loading ratio C can actually increase above 150 because of the gas density decrease to $\rho_g = 4\,\mathrm{kg/m^3}$ in the entrainment region, bringing the characteristic time of the two-way coupled drag system close to $\tau_c^{\boldsymbol{u}} = 8\,\mathrm{ns}$. The low numerical dissipation of Raptor does a good job in resolving a significant amount of the turbulence induced by the jet. In this way, the intermediate-scale structures of the jet, believed to participate in driving the mixing, ignition, and combustion processes, are correctly captured.

5.2.3 Case with $T_g = 1200\,\mathbf{K}$

This corresponds to a case where ignition takes place earlier and closer to the injector compared to the 900 K-case. The gas temperature and fuel vapor mass fraction after $t_2 = 60\,\mu\mathrm{m}$ are shown in Fig. 5.6. The fuel vapor mass fraction, together with the level of turbulence and the temperature of the mixture, is considered to be a driver of autoignition [45, 37, 29]. These results are promising for analyzing autoignition, its mechanisms, and its statistics.

We remark that this test case was carried out with 1600 cores. No particular optimization was sought for parallel computing besides relying on the scalability of Raptor and the intrinsic load-balancing properties of the FSL-LP method. The overall parallel efficiency of Raptor, when coupled with the Multi-Fluid solver, was satisfactory: even with frequent outputs, the wall clock time was less than a day of computation.

5.3 Reacting polydisperse LES of Spray A

5.3.1 Setup

To demonstrate the full modeling strategy, the reacting version of Spray A is finally presented with a polydisperse model for the disperse phase. According to Spray A specifications, the chamber ($T_g = 900\,\mathrm{K}$, $P_g = 6\,\mathrm{MPa}$) is filled with a mixture of the burnt gases left by the preheating with molar fractions O_2: 15.00%, N_2: 75.15%, CO_2: 6.22%, H_2O: 3.62%, and density $\rho_g = 22.8\,\mathrm{kg/m^3}$. The chemical reaction model is a two-step mechanism optimized for autoignition through statistical calibration [37]. The geometry is now a box of size $54 \times 10.8 \times 10.8\,\mathrm{mm^3}$ to include the entire spray region at typical auto-ignition time. It is discretized as a cartesian mesh of $1200 \times 240 \times 240$ cells, which translates to 2 cells per nozzle diameter. All the characteristics of this computation are summed up in the right column of Table 5.1.

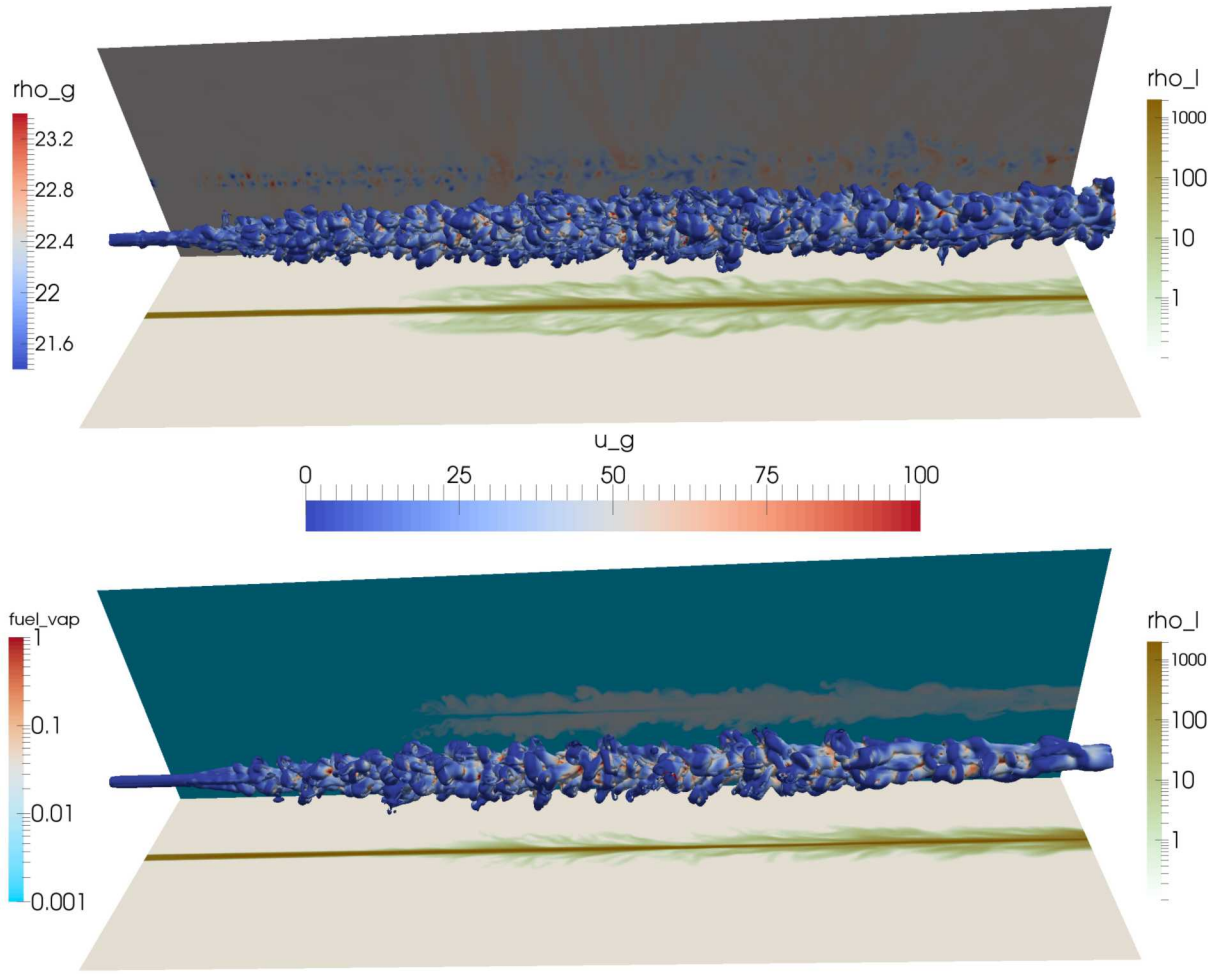

Figure 5.5. Near-nozzle monodisperse spray A case ($T_g = 900\,\mathrm{K}$) after $t_1 = 28\,\mu\mathrm{s}$. Isocontour of gas vorticity norm colored by gas axial velocity u_g. Bottom plane shows the liquid density at horizontal centerplane slice. Top: Case without evaporation, back plane showing gas density at vertical centerplane slice; Bottom: Case with evaporation, back plane showing fuel vapor mass fraction at vertical centerplane slice.

5.3.2 Disperse-phase initial conditions

A laminar plug-flow profile is used for the fuel jet with a velocity ramp matching the measured rate of injection [4]; n-dodecane ($\rho_l = 702\,\mathrm{kg/m^3}$, $T_l = 363\,\mathrm{K}$) is injected as a round jet of liquid drops at a speed of $\boldsymbol{u}_l(t, \boldsymbol{x}_0) = 600\,\mathrm{m/s}$. The angle $\alpha_0 = 6\,\mathrm{deg}$ between the injected drop velocities and the injection axis is prescribed so that drop trajectories spread conically from the axis. This one parameter comes from a simplified approach to describe the spreading of the spray due to turbulence and early atomization in order to match the spray angle. The drop sizes are prescribed from the lognormal distribution found in Section 4.1; the distribution is then discretized using the

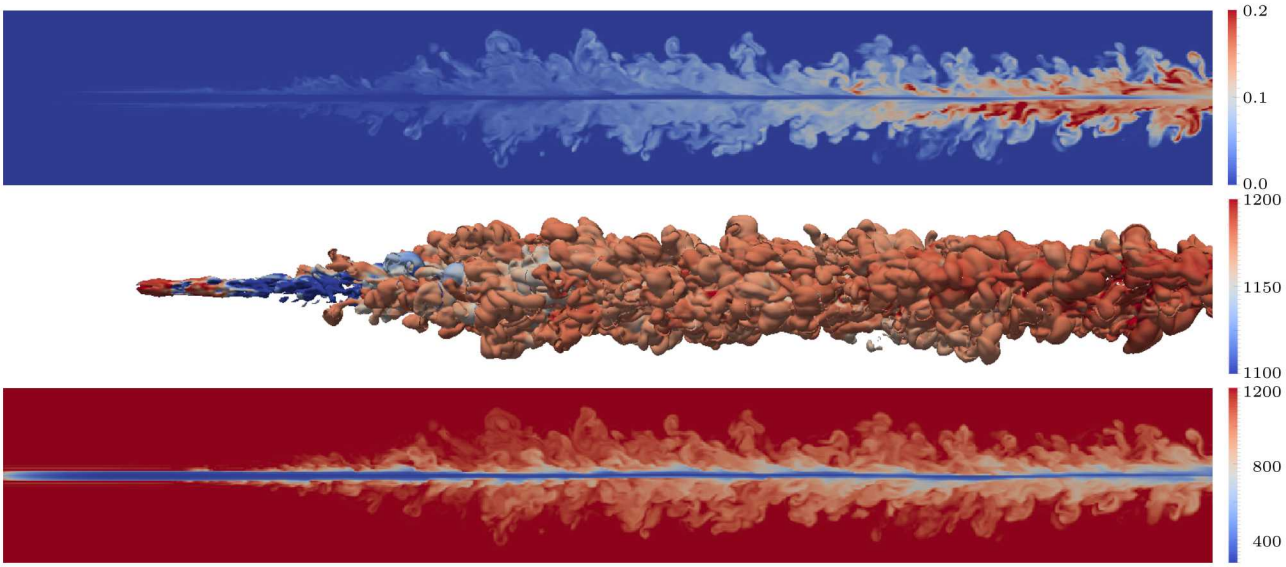

Figure 5.6. Near-nozzle monodisperse spray A case (T_g = 1200 K) with evaporation after t_2 = 60 μs. Top: Fuel vapor mass fraction at centerplane; Middle: Fuel vapor isocontour with $Y_{C_{12}H_{26}} = 0.01$; Bottom: Gas temperature at centerplane.

two-size moment sectional method. The characteristics of the three sections are given in Table 5.2. Their bounds are chosen to reflect the different dynamics of tracers, low inertia, and moderate inertia drops that is relevant in direct fuel injection. This two-size moment discretization preserves the mass flow rate ratios and the average $r_{30,k}$ of the lognormal distribution in each section.

Section number	1	2	3
Upper bound (μm)	6	9.5	11.7
Initial average radius $r_{30,k}$ (μm)	3.88	7.37	11.68
Mass flow rate ratio	30.9%	34.3%	30.8%
Drag characteristic time (μs)	54	196	493

Table 5.2. Sectional discretization parameters as a model for the lognormal fit ($\mu_{LN} = 1.9608$ and $\sigma_{LN} = 0.4495$) to the average size distribution obtained with a CLSVOF atomization DNS.

.

5.3.3 Far-field spray behavior

The time evolution of the flow is presented in Fig. 5.7 and compares well to the behavior of Diesel sprays, with a rapid initial penetration followed by the slower development of the vapor-rich turbulent region. The behavior of the liquid phase is displayed in Fig. 5.8. It can be seen that the dense core behaves similarly for the three sections, while the sections respond with a

different dynamics to the downstream vortices as soon as their mass loading is about or below 10% ($\approx$ 70kg/m^3). The general aspects of entrainment and turbulence generation are retrieved as a result of the simultaneous coupling of all sections and gas through the splitting strategy.

5.3.4 Thermochemistry analysis

The fields of fuel vapor and CO, an intermediate reacting species, are given in Fig. 5.9. They extend beyond the liquid spray region and match the domain where the Q-criterion indicates a high level of turbulence. Both these fields are corrugated and CO is significantly produced at the downstream end of the plume. Together with the equivalence ratio and temperature of Fig. 5.10, these diagrams enable the study of the mechanisms that lead to autoignition. In particular, we note that the end of the plume has a large region where the temperature is above 800 K and the equivalence ratio φ is close to 2. At this temperature, high equivalence ratios are known to favor the so-called low-temperature reactions of the fuel, therefore this rich region is a major candidate to investigate the path to autoignition [45, 37, 29].

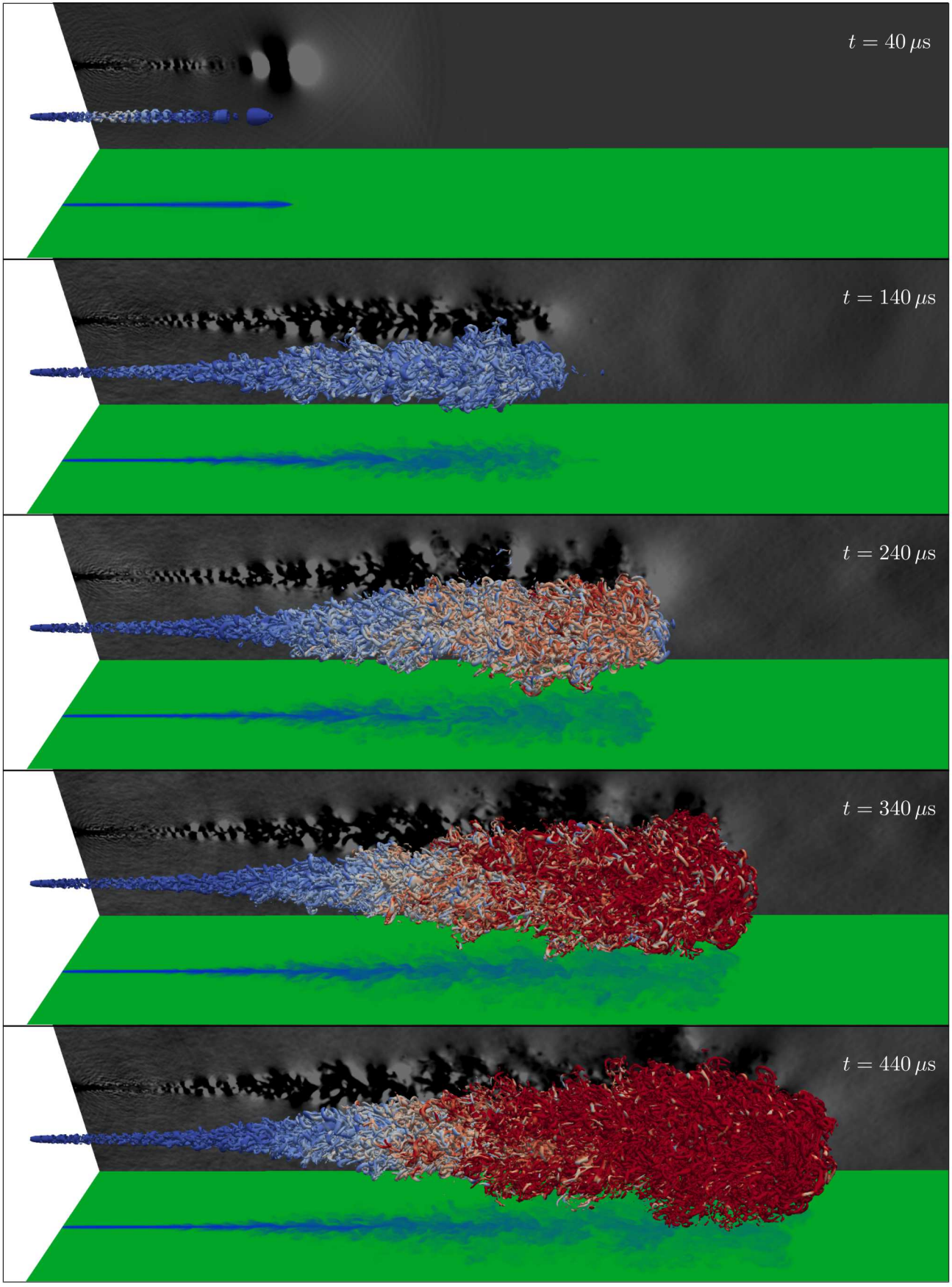

Figure 5.7. Injection sequence showing isocontour of Q-criterion colored by CO mass fraction (blue: 0%; red: 0.1%); Back plane: Gas pressure in the vertical center plane; Bottom plane: Gas temperature in the horizontal center plane.

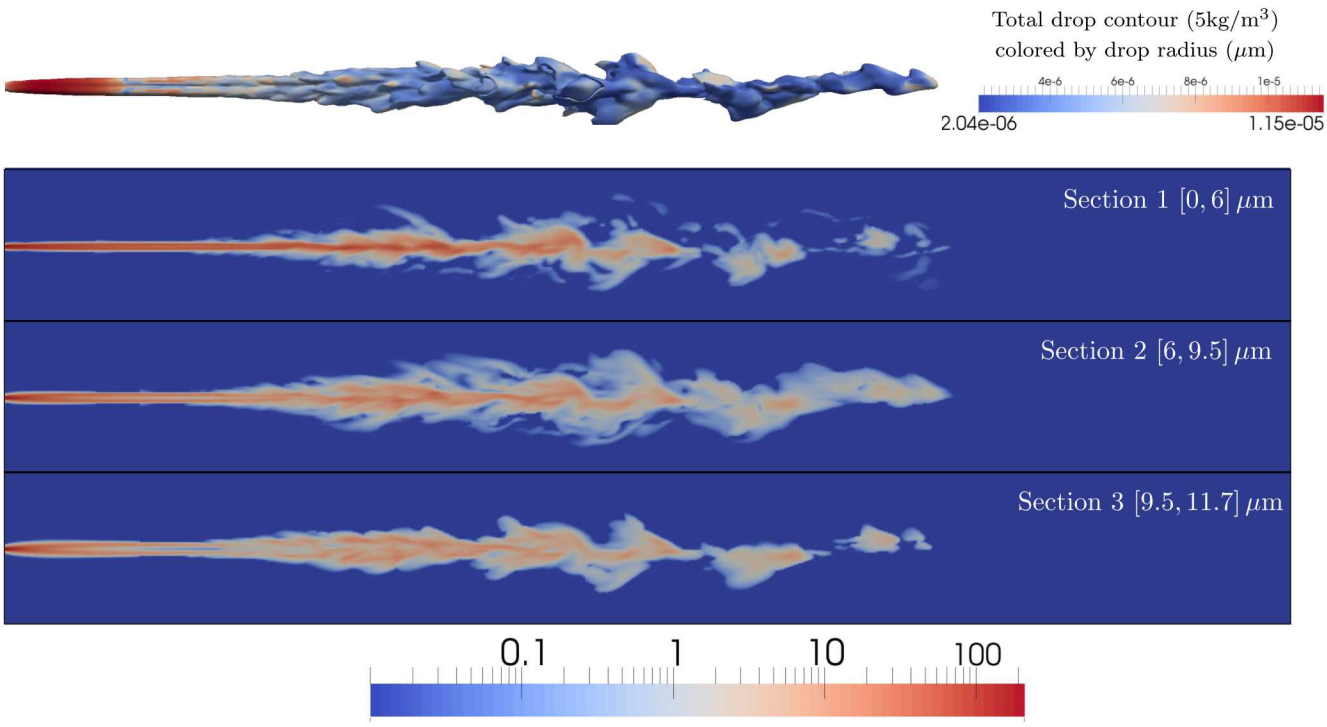

Figure 5.8. Spray mass density (kg/m^3) in the reacting jet case at $t_0 = 400\,\mu$s.

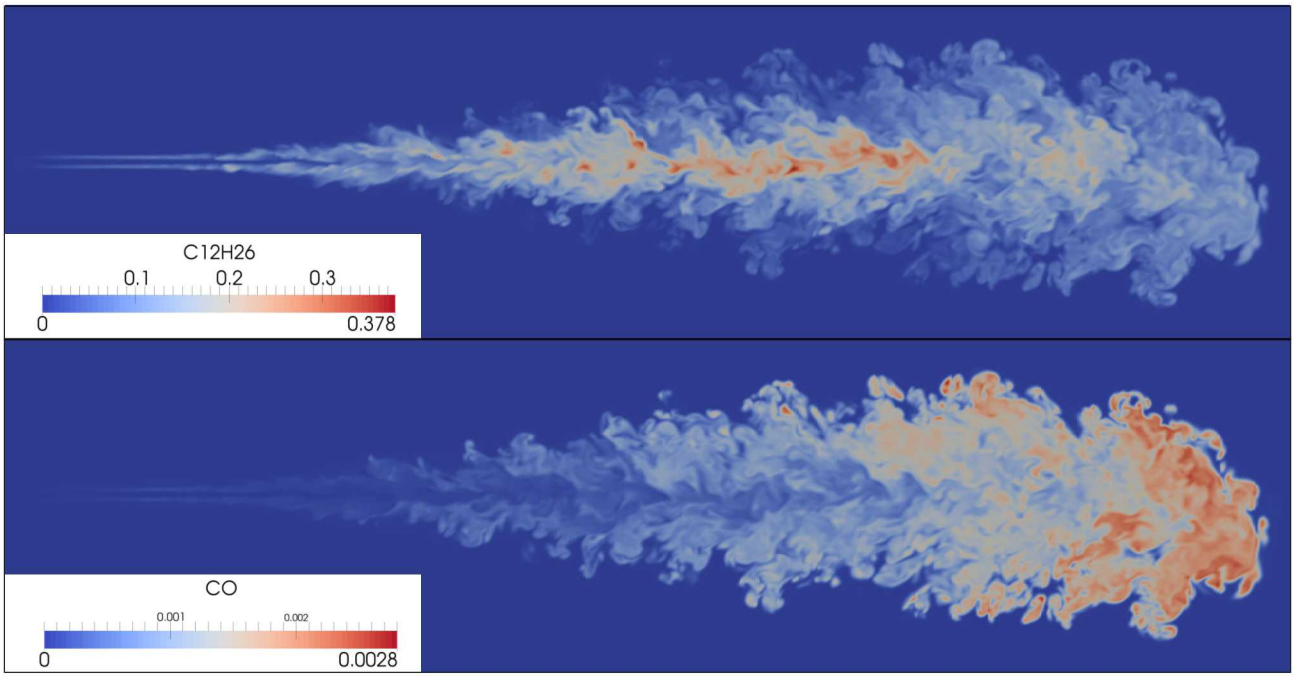

Figure 5.9. Fuel species in the reacting jet case at $t_0 = 400\,\mu$s; Top: n-dodecane; Bottom: carbon monoxide.

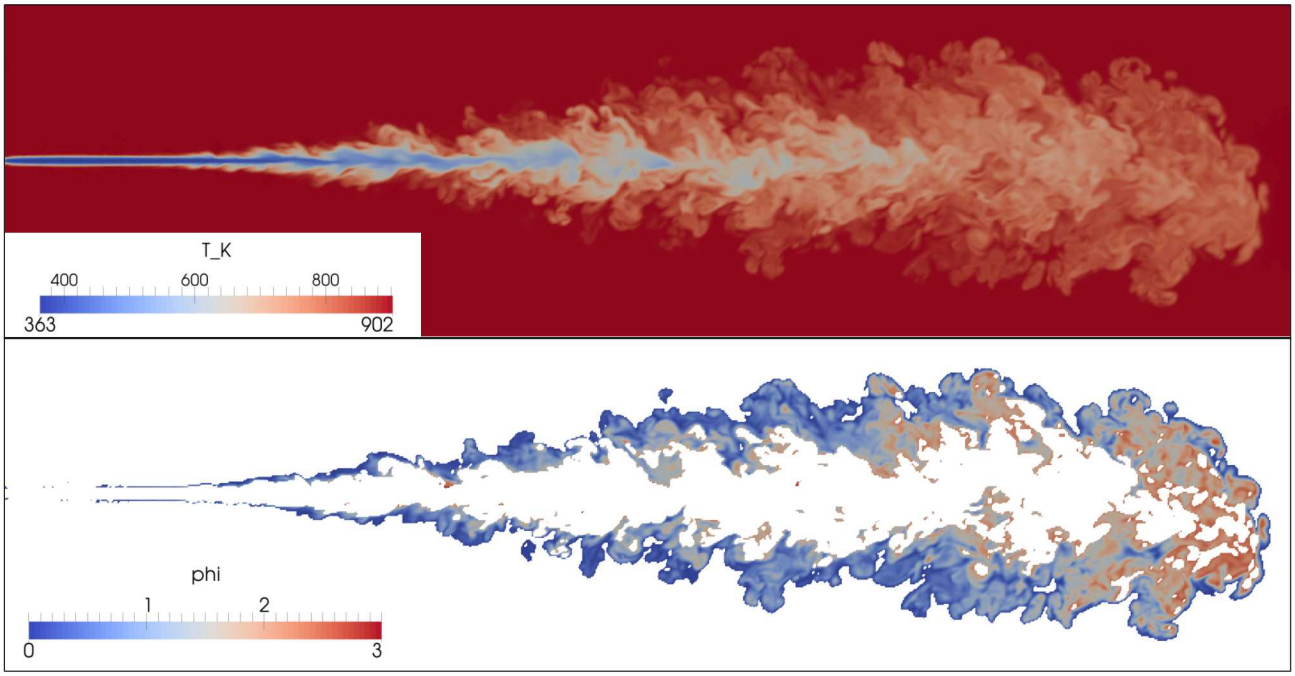

Figure 5.10. Thermochemistry fields in the reacting jet case at $t_0 = 400\,\mu$s; Top: gas temperature; Bottom: equivalence ratio φ after temperature masking with $800K < T_g < 899K$.

Chapter 6

Conclusion and path forward

6.1 Prospects for LES of atomization

We have demonstrated that the proposed Eulerian Multi-Phase coupling is robust and scalable for dense sprays. Moreover, simple EMF closure terms for mass, momentum and energy exchange behave reasonably well in the near-nozzle region because it appears that the sensitivity of the coupling source terms to the prescribed droplet size is relatively small there. There are, however, limitations in the current approach. The liquid compressibility in the spray core is not properly rendered: the liquid phase density at very high loading is not controlled and can reach non-physical values. In addition, surface tension is not accounted for. This terms drives large scale dynamics (Rayleigh-Taylor, Rayleigh-Plateau instabilities, jet and sheet flapping) at relatively low Reynolds and Weber numbers, but it is uncertain how to introduce surface tension effects in fully turbulent liquid break-up. Both issues could be controlled by adding inter-particle interactions in the Lagrangian transport step of the algorithm – specifically, a repulsive force to control density and an attractive force to mimic surface tension. But it is not known at this point what effect could these additions have on the robustness of the coupling algorithm and its computational cost. There are also limitation in our current model of direct fuel injection within the LES framework, namely the inclusion of collision, coalescence, and break-up models in the transition from dense to dilute spray. Some of these aspects could be handled by existing sub-models, which have not been implemented yet in the coupling code; others are the matter of ongoing research. To the latter group belongs the determination of the spray field from primary atomization. This field is the result of interface-dominated small-scale interactions and needs to be prescribed by an external simulation, CLSVOF for this project. The challenge is that, in describing the turbulent dynamics of the gas-liquid interface, the smallest scale of motion are not known *a priori*, contrary to the Kolmogorov and the Bachelor scales that are defined in single-phase flow. Subgrid models in LES are generally based on gradients that originate from the large-scale turbulence field and not from the presence of an interface. Simulations have recently been attempted (see, for instance, [73]) based on the assumption that large-scale features of the flow do not depend on surface tension or on viscosity and that subgrid algebraic stress models can be used as long as they account for the effect of the liquid-gas density ratio [67]. As many aspects of this or of similar approaches have not been rigorously tested, an investigation of this topic would be the natural continuation of this project.

References

[1] M. Arienti and M. Sussman. Numerical study of the thermal transient in high-pressure diesel injection. *to appear in Int. J. Multiph. Flows.*

[2] M. Arienti and M. Sussman. A High-Fidelity Study of High-Pressure Diesel Injection. *SAE Tech. Paper 01-1853*, 2015.

[3] M. Arienti, X. Li, M.C Soteriou, C. A. Eckett, M. Sussman, and R. J. Jensen. Coupled level-set/volume-of-fluid method for simulation of injector atomization. *J. Prop. Power*, 29(1): 147–157, 2013.

[4] M. Bardi, R. Payri, L.-M. Malbec, G. Bruneaux, L. M. Pickett, J. Manin, T. Bazyn, and C. Genzale. Engine Combustion Network: comparison of spray development, vaporization, and combustion in different combustion vessels. *Atom. Spr.*, 22(10), 2012.

[5] A. Bernard-Champmartin, J.-P. Braeunig, C. Fochesato, and T. Goudon. A semi-Lagrangian approach for dilute non-collisional fluid-particle flows. *Communications in Computational Physics*, 19(3):801–840, 2016.

[6] N. Besse. Convergence of a semi-Lagrangian scheme for the one-dimensional Vlasov–Poisson system. *SIAM Journal on Numerical Analysis*, 42(1):350–382, 2004.

[7] G. A. Bird. *Molecular gas dynamics and the direct simulation of gas flows*, volume 42. Oxford Science Publications, 1994.

[8] M. Boileau, G. Staffelbach, B. Cuenot, T. Poinsot, and C. Bérat. LES of an ignition sequence in a gas turbine engine. *Comb. Flame*, 154(1):2–22, 2008.

[9] F. Bouchut. On zero pressure gas dynamics. In *Advances in kinetic theory and computing*, pages 171–190. World Sci. Publishing, River Edge, NJ, 1994.

[10] F. Bouchut, S. Jin, and X. Li. Numerical approximations of pressureless and isothermal gas dynamics. *SIAM J. Num. Anal.*, 41:135–158, 2003.

[11] C. Chalons, M. Massot, and A. Vié. On the Eulerian Large Eddy Simulation of disperse phase flows: an asymptotic preserving scheme for small Stokes number flows. *Multiscale Modeling & Simulation*, 13(1):291–315, 2015.

[12] C.-Z. Cheng and G. Knorr. The integration of the Vlasov equation in configuration space. *J. Comp. Phys.*, 22(3):330–351, 1976.

[13] B. Cockburn, G. E. Karniadikis, and C. W. Shu. *Discontinuous Galerkin Methods - Theory, Computation, and Applications*, volume 11 of *Lecture Notes in Computer Science and Engineering*. Springer Verlag, New York, 2000.

[14] G.-H. Cottet, J.-M. Etancelin, F. Pérignon, and C. Picard. High order semi-Lagrangian particle methods for transport equations: numerical analysis and implementation issues. *ESAIM. Mathematical Modelling and Numerical Analysis*, 48(4):1029, 2014.

[15] R. Courant, E. Isaacson, and M. Rees. On the solution of nonlinear hyperbolic differential equations by finite differences. *Communications on Pure and Applied Mathematics*, 5(3):243–255, 1952.

[16] N. Crouseilles, T. Respaud, and E. Sonnendrücker. A forward semi-lagrangian method for the numerical solution of the Vlasov equation. *Computer Physics Communications*, 180(10): 1730–1745, 2009.

[17] C. Crua, G. de Sercey, M. R. Heikal, and Gold M. Dropsizing of near-nozzle diesel and rme sprays by microscopic imaging. In *ILASS Americas 12th ILASS.*, 2012.

[18] R.N. Dahms and J.C. Oefelein. On the transition between two-phase and single-phase interface dynamics in multicomponent fluids at supercritical pressures. *Phys. Fluids*, 25(9):092103, 2013.

[19] R.N. Dahms, J. Manin, L.M. Pickett, and J.C. Oefelein. Understanding high-pressure gas-liquid interface phenomena in diesel engines. *Proc. Comb. Inst.*, 34(1):1667–1675, 2013.

[20] S. de Chaisemartin. *Polydisperse evaporating spray turbulent dispersion: Eulerian model and numerical simulation.* PhD thesis, Ecole Centrale Paris, 2009.

[21] Jacques Denavit. Numerical simulation of plasmas with periodic smoothing in phase space. *J. Comp. Phys.*, 9(1):75–98, 1972.

[22] S. Descombes and M. Massot. Operator splitting for nonlinear reaction-diffusion systems with an entropic structure: singular perturbation and order reduction. *Num. Math.*, 97(4):667–698, 2004. ISSN 0029-599X.

[23] F. Doisneau. *Eulerian modeling and simulation of polydisperse moderately dense coalescing spray flows with nanometric-to-inertial droplets: application to Solid Rocket Motors.* PhD thesis, École Centrale Paris, 2013.

[24] F. Doisneau, J. Dupays, A. Murrone, F. Laurent, and M. Massot. Eulerian VS Lagrangian simulation of unsteady two-way coupled coalescing two-phase flows in solid propellant combustion. *C. R. Mec.*, 341:44–54, 2013. Special issue "Combustion, spray and flow dynamics for aerospace propulsion".

[25] F. Doisneau, F. Laurent, A. Murrone, J. Dupays, and M. Massot. Eulerian Multi-Fluid models for the simulation of dynamics and coalescence of particles in solid propellant combustion. *J. Comp. Phys.*, 234:230–262, 2013.

[26] F. Doisneau, A. Sibra, J. Dupays, A. Murrone, F. Laurent, and M. Massot. Numerical strategy for unsteady two-way coupled polydisperse sprays: Application to solid-rocket instabilities. *J. Prop. Power*, 30(3):727–747, 2014.

[27] F. Doisneau, M. Arienti, and J. C. Oefelein. Space-filtered kinetic theory for the LES of dense sprays. In *13th ICLASS*, pages 1–12, Tainan, Taiwan, 2015.

[28] F. Doisneau, M. Arienti, and J. C. Oefelein. A semi-Lagrangian transport method for kinetic problems with application to dense-to-dilute polydisperse reacting spray flows. *J. Comp. Phys.*, pages 1–30, 2016. Accepted.

[29] F. Doisneau, M. Arienti, and J. C. Oefelein. On Multi-Fluid models for spray-resolved LES of reacting jets. *Proc. Comb. Inst.*, pages 1–9, 2017. Accepted.

[30] O. Emre, R.O. Fox, M. Massot, S. De Chaisemartin, S. Jay, and F. Laurent. Towards eulerian modeling of a polydisperse evaporating spray under realistic internal-combustion-engine conditions. *Flow. Turb. Comb.*, 93(4):689–722, 2014.

[31] O. Emre, D. Kah, S. Jay, Q.-H. Tran, A. Velghe, S. De Chaisemartin, R.O. Fox, F. Laurent, and M. Massot. Eulerian moment methods for automotive sprays. *Atomization and Sprays*, 25(3), 2015.

[32] M. Falcone and R. Ferretti. *Semi-Lagrangian approximation schemes for linear and Hamilton-Jacobi equations*. Cambridge University Press, 2014.

[33] P. Fede, O. Simonin, and A. Ingram. 3D numerical simulation of a lab-scale pressurized dense fluidized bed focussing on the effect of the particle-particle restitution coefficient and particle–wall boundary conditions. *Chemical Engineering Science*, 142:215–235, 2016.

[34] R. O. Fox. On multiphase turbulence models for collisional fluid–particle flows. *J. Fluid Mech.*, 742:368–424, 2014.

[35] S.K. Godunov. A difference method for numerical calculation of discontinuous solutions of the equations of hydrodynamics. *Matematicheskii Sbornik*, 47(3):271–306, 1959.

[36] V. Grandgirard, M. Brunetti, P. Bertrand, N. Besse, X. Garbet, P. Ghendrih, G. Manfredi, Y. Sarazin, O. Sauter, and E. Sonnendrücker. A drift-kinetic semi-Lagrangian 4D code for ion turbulence simulation. *J. Comp. Phys.*, 217(2):395–423, 2006.

[37] L. Hakim, G. Lacaze, M. Khalil, H.N. Najm, and J.C. Oefelein. Modeling Auto-Ignition Transients in Reacting Diesel Jets. *J. Eng. Gas Turb. Power*, 138(11):112806, 2016.

[38] A. Hamiaz, M. Mehrenberger, H. Sellama, and E. Sonnendrücker. The semi-Lagrangian method on curvilinear grids. 2015. Available on hal.archives-ouvertes.fr.

[39] A. Hamiaz, M. Mehrenberger, A. Back, and P. Navaro. Guiding center simulations on curvilinear grids. *ESAIM. Proceedings and Surveys*, 53, 2016.

[40] M. Herrmann. A parallel eulerian interface tracking/lagrangian point particle multi-scale coupling procedure. *J. Comp. Phys.*, 229(3):745–759, 2010.

[41] M. Jemison, M. Sussman, and M. Arienti. Compressible, multiphase semi-implicit method with moment of fluid interface representation. *J. Comp. Phys.*, 279:182–217, 2014.

[42] D. Kah, O. Emre, Q.H. Tran, S. Chaisemartin, S. Jay, F. Laurent, and M. Massot. High order moment method for polydisperse evaporating sprays with mesh movement: Application to internal combustion engines. *Int. J. Multiph. Flows*, 71:38–65, 2015.

[43] C. Klingenberg and K. Waagan. Relaxation solvers for ideal MHD equations-a review. *Acta Mathematica Scientia*, 30(2):621–632, 2010.

[44] T. N. Krishnamurti. Numerical integration of primitive equations by a quasi-Lagrangian advective scheme. *Journal of applied Meteorology*, 1(4):508–521, 1962.

[45] G. Lacaze, A. Misdariis, A. Ruiz, and J.C. Oefelein. Analysis of high-pressure Diesel fuel injection processes using LES with real-fluid thermodynamics and transport. *Proc. Comb. Inst.*, 2015.

[46] F. Laurent and M. Massot. Multi-fluid modeling of laminar poly-dispersed spray flames: origin, assumptions and comparison of the sectional and sampling methods. *Comb. Th. Model.*, 5: 537–572, 2001.

[47] F. Laurent, A. Sibra, and F. Doisneau. Two-size moment multi-fluid model: a robust and high-fidelity description of polydisperse moderately dense evaporating sprays. *Accepted for publication in Comm. Comp. Phys.*, 2016.

[48] A. Magni and G.H. Cottet. Accurate, non-oscillatory, remeshing schemes for particle methods. *J. Comp. Phys.*, 231(1):152–172, 2012.

[49] L. Martinez, A. Benkenida, and B. Cuenot. A model for the injection boundary conditions in the context of 3D simulation of Diesel spray: methodology and validation. *Fuel*, 89:219–228, 2010.

[50] T. Menard, S. Tanguy, and A. Berlemont. Coupling level set/VOF/ghost fluid methods: Validation and application to 3D simulation of the primary break-up of a liquid jet. *Int. J. Multiph. Flows*, 33(5):510–524, 2007.

[51] R. D. Nair, J. S. Scroggs, and F. H. M. Semazzi. A forward-trajectory global semi-Lagrangian transport scheme. *J. Comp. Phys.*, 190(1):275–294, 2003.

[52] J. C. Oefelein. Large Eddy Simulation of turbulent combustion processes in propulsion and power systems. *Prog. Aerosp. Sc.*, 42(1):2–37, 2006.

[53] R. Paoli, T. Poinsot, and K. Shariff. Testing semi-Lagrangian schemes for two-phase flow applications. In *Proceeding of the Summer Program*. Stanford CTR, 2006.

[54] C.F. Powell, M. Smooke D. Duke, and M. Baum. Measurement of diesel spray droplet size with ultra-small angle x-ray scattering. In *ILASS Americas 25th ILASSPittsburgh, PA.*, 2013.

[55] T. Respaud and E. Sonnendrücker. Analysis of a new class of forward semi-Lagrangian schemes for the 1D Vlasov-Poisson equations. *Numerische Mathematik*, 118(2):329–366, 2011.

[56] J. Reveillon and F.X. Demoulin. Effects of the preferential segregation of droplets on evaporation and turbulent mixing. *J. Fluid Mech.*, 583:273–302, 2007.

[57] A. Robert. A semi-Lagrangian and semi-implicit numerical integration scheme for the primitive meteorological equations. *J. Meteor. Soc. Jap.*, 60(1):319–325, 1982.

[58] M. Sabat, A. Larat, A. Vié, and M. Massot. On the development of high order realizable schemes for the Eulerian simulation of disperse phase flows : a convex-state preserving Discontinuous Galerkin method. *J. Comp. Multiphase Flows*, 6(3):247–270, 2014.

[59] C.W. Shu and S. Osher. Efficient implementation of essentially non-oscillatory shock-capturing schemes. *J. Comp. Phys.*, 77(2):439–471, 1988.

[60] A. Sibra, J. Dupays, F. Laurent, and M. Massot. A new Eulerian Multi-Fluid model for bi-component polydisperse sprays: an essential approach to evaluate the impact of aluminum combustion on Solid Rocket Motor instabilities. In 49^{th} *AIAA/ASME/SAE/ASEE Joint Propulsion Conference*, pages 1–20, San Jose, Ca, 2013.

[61] P. K. Smolarkiewicz and J. A. Pudykiewicz. A class of semi-Lagrangian approximations for fluids. *J. Atm. Sc.*, 49(22):2082–2096, 1992.

[62] E. Sonnendrücker, J. Roche, P. Bertrand, and A. Ghizzo. The semi-Lagrangian method for the numerical resolution of the Vlasov equation. *J. Comp. Phys.*, 149(2):201–220, 1999.

[63] A. Staniforth and J. Côté. Semi-Lagrangian integration schemes for atmospheric models-a review. *Monthly Weather Review*, 119(9):2206–2223, 1991.

[64] S. Subramaniam. Lagrangian–Eulerian methods for multiphase flows. *Prog. Ener. Comb. Sc.*, 39(2):215–245, 2013.

[65] O. Thomine. *Développement de méthodes multi-échelles pour la simulation numérique des écoulements réactifs diphasiques*. PhD thesis, Université de Rouen, 2011.

[66] J. Tillou, J.-B. Michel, C. Angelberger, and D. Veynante. Assessing LES models based on tabulated chemistry for the simulation of diesel spray combustion. *Comb. Flame*, 161(2): 525–540, 2014.

[67] A. Vallet, AA Burluka, and R. Borghi. Development of a Eulerian model for the "atomization" of a liquid jet. *Atom. Spr.*, 11(6):619–642, 2001.

[68] B. Van Leer. Toward the ultimate conservation difference scheme V. a second-order sequel to Godunov's method. *J. Comp. Phys.*, 32(1):101–136, 1979.

[69] A. Vié, F. Doisneau, and M. Massot. On the Anisotropic Gaussian velocity closure for inertial-particle laden flows. *Comm. Comp. Phys.*, 17:1–46, 2015.

[70] K. Waagan, C. Federrath, and C. Klingenberg. A robust numerical scheme for highly compressible magnetohydrodynamics: Nonlinear stability, implementation and tests. *J. Comp. Phys.*, 230(9):3331–3351, 2011.

[71] A Wiin-Nielsen. On the application of trajectory methods in numerical forecasting. *Tellus*, 11 (2):180–196, 1959.

[72] F. A. Williams. Spray combustion and atomization. *Phys. Fluids*, 1:541–545, 1958.

[73] Q. Xue, S. Som, P. K. Senecal, and E. Pomraning. Large eddy simulation of fuel-spray under non-reacting ic engine conditions. *Atom. Spr.*, 23(10), 2013.

[74] C. Yuan and R.O. Fox. Conditional quadrature method of moments for kinetic equations. *J. Comp. Phys.*, 230(22):8216–8246, 2011.

[75] Y. B. Zel′dovich. Gravitational instability : an approximate theory for large density perturbations. *Astronomy and Astrophysics*, 5:84–89, 1970.

DISTRIBUTION:

	MS	,
		,
1	MS 0899	Technical Library, 9536 (electronic copy)

Sandia National Laboratories is a multimission laboratory managed and operated by National Technology & Engineering Solutions of Sandia, LLC, a wholly owned subsidiary of Honeywell International Inc., for the U.S. Department of Energy's National Nuclear Security Administration under contract DE-NA0003525.